AGU PUBLICATIONS

Geochemistry, Geophysics, Geosystems

RESEARCH ARTICLE
10.1002/2014GC005477

Key Points:
- Central volcanoes form by focused, high efussion rate eruptions
- Axial graben forms as melt supply is reduced, bisecting the central volcano
- Central volcanoes impart along-axis variations in mode of crustal accretion

Supporting Information:
- Readme
- Figures S1a, S1b
- Faults_Eastward
- Faults_Westward
- Fissures

Correspondence to:
J. Escartín,
escartin@ipgp.fr

Citation:
Escartín, J., S. A. Soule, M. Cannat, D. J. Fornari, D. Düşünür, and R. Garcia (2014), Lucky Strike seamount: Implications for the emplacement and rifting of segment-centered volcanoes at slow spreading mid-ocean ridges, *Geochem. Geophys. Geosyst.*, *15*, 4157–4179, doi:10.1002/2014GC005477.

Received 26 JUN 2014
Accepted 10 OCT 2014
Accepted article online 14 OCT 2014
Published online 7 NOV 2014

Lucky Strike seamount: Implications for the emplacement and rifting of segment-centered volcanoes at slow spreading mid-ocean ridges

J. Escartín[1], S. A. Soule[2], M. Cannat[1], D. J. Fornari[2], D. Düşünür[3], and R. Garcia[4]

[1]Groupe de Géosciences Marines, IPGP, CNRS UMR 7154, Paris, France, [2]Department of Geology and Geophysics, Woods Hole Oceanographic Institution, Woods Hole, Massachusetts, USA, [3]Department of Geophysical Engineering, Istambul Technical University, Istambul, Turkey, [4]Computer Vision and Robotics Group, University of Girona, Girona, Spain

Abstract The history of emplacement, tectonic evolution, and dismemberment of a central volcano within the rift valley of the slow spreading Mid-Atlantic Ridge at the Lucky Strike Segment is deduced using near-bottom sidescan sonar imagery and visual observations. Volcano emplacement is rapid (<1 Myr), associated with focused eruptions, and with effusion rates feeding lava flows that bury tectonic features developed prior to and during volcano construction. This volcanic phase likely requires efficient melt pooling and a long-lived crustal magma chamber as a melt source. A reduction in melt supply triggers formation of an axial graben rifting the central volcano, and the onset of seafloor spreading may eventually split it. At Lucky Strike, this results in two modes of crustal construction. Eruptions and tectonic activity focus at a narrow graben that bisects the central volcano and contains the youngest lava flows, accumulating a thick layer of extrusives. Away from the volcano summit, deformation and volcanic emplacement is distributed throughout the rift valley floor, lacking a clear locus of accretion and deformation. Volcanic emplacement on the rift floor is characterized by axial volcanic ridges fed by dikes that propagate from the central axial magma chamber. The mode of rapid volcano construction and subsequent rifting observed at the Lucky Strike seamount is common at other central volcanoes along the global mid-ocean ridge system.

1. Introduction

Slow spreading ridges display a large variability in the mode of crustal accretion owing to changes in magma supply and the amount and style of tectonic extension. Linear ridge segments, extending tens of kilometers along axis, display features suggesting robust melt supply and its focusing at segment centers [*Kuo and Forysth*, 1988; *Lin et al*., 1990], where the crust is thickest [e.g., *Detrick et al*., 1995; *Hooft et al*., 2000; *Magde et al*., 2000; *Minshull et al*., 1995]. This melt may be redistributed along axis, toward the segment ends by diking. Volcanic activity within the rift valley floor results in the emplacement of axial volcanic ridges and small volcanic cones, variably crosscut by faults and fissures [*Cann and Smith*, 2005; *Searle et al*., 2010; *Smith and Cann*, 1993]. The centers of magmatic segments often host hydrothermal fields such as those along the MAR at Menez Gwen (38°20′N) and Lucky Strike (37°50′N) [*Fouquet et al*., 1994; *Langmuir et al*., 1997; *Ondreas et al*., 1997; *Charlou et al*., 2000], likely driven by an underlying melt lens such as the 3 km deep lens below the Lucky Strike field [*Singh et al*., 2006]. Emplacement of large central volcanoes within the rift valley is an extreme manifestation of melt focusing, and is common at the midpoints of segments at slow spreading ridges such as the Mid-Atlantic Ridge (MAR) [*Ondreas et al*., 1997] or the ultraslow Arctic [e.g., *Okino et al*., 2002; *Michael et al*., 2003] and South-West Indian Ridges (SWIR) [*Dick et al*., 2003; *Sauter et al*., 2004]. These volcanic edifices rise a few hundred meters to more than a kilometer above the rift valley floor, and have basal diameters that may exceed 10 km.

Formation of central volcanoes requires melt pooling within the middle to lower crust and upper mantle, and a localized eruption at the seafloor of large volumes of melt. Individual volcanoes are underlain by thick crust as inferred from prominent mantle Bouguer gravity lows [*Cannat et al*., 1999a, 1999b; *Escartín et al*., 2001; *Sauter and Cannat*, 2010], consistent with melt focusing. A similar organization of melt supply focused to a central volcano is observed at subaerial sections of the Mid-Atlantic Ridge in Iceland [*Arnott and Foulger*, 1994b, 1994b], and at continental rift zones [*de Chabalier and Avouac*, 1994; *Ebinger and Casey*,

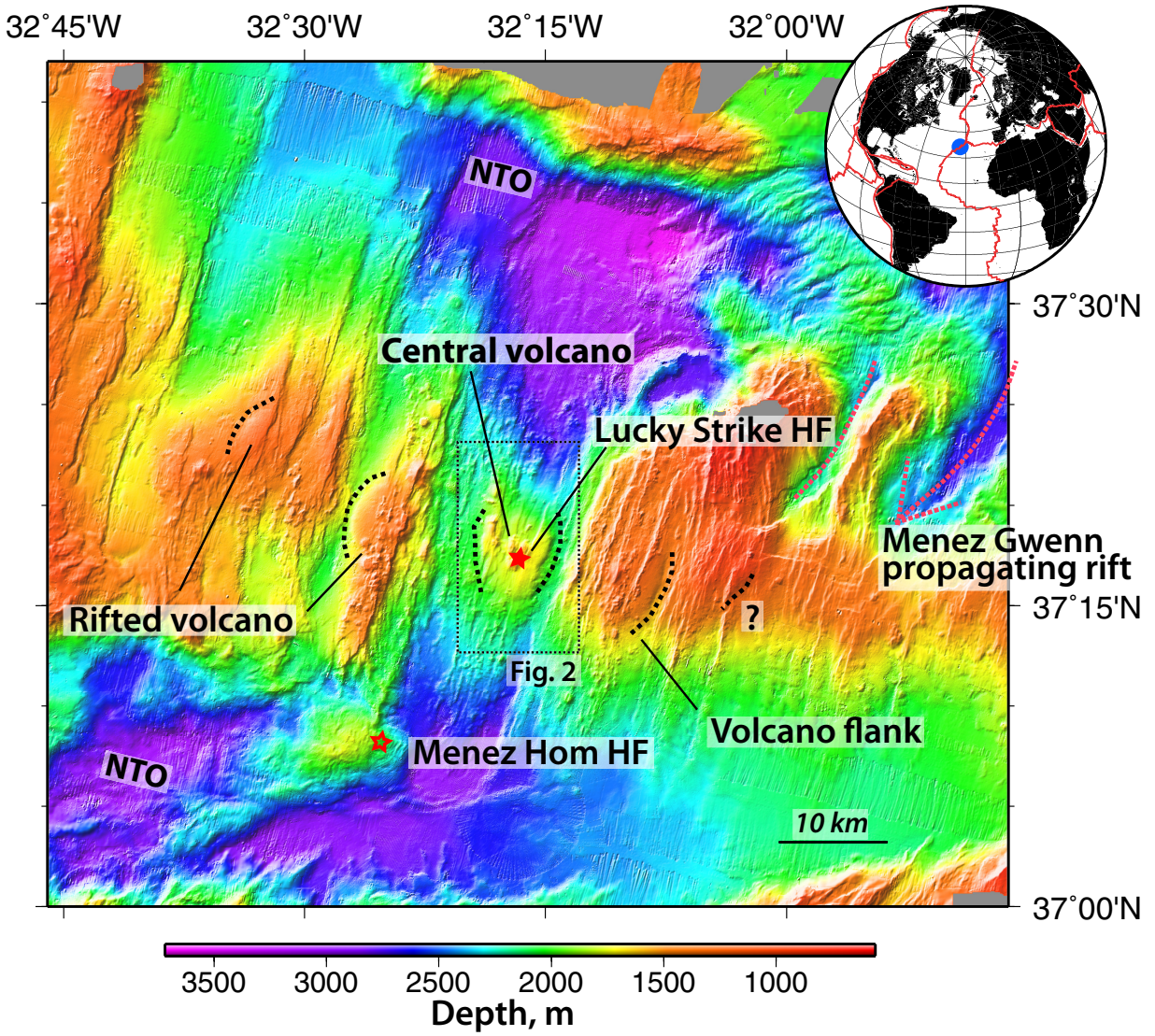

Figure 1. Bathymetry of the Lucky Strike segment and flanking seafloor. A succession of rifted central volcanoes, with well-preserved edges (dashed black lines) extend off axis from the present-day central volcano that hosts the Lucky Strike hydrothermal field. Nontransform offsets (NTO) show a complex structure with tectonic rotation, faulting, and uplift. The northern end of the Lucky Strike segment overlaps with extensional rifts to the East, formed during the southward propagation of the Menez Gwen segment (dashed red lines). The southern massif (Menez Hom) yields ultramafic rocks [*Ribeiro da Costa*, 2008] and anomalies in the water column suggesting active serpentinization-related hydrothermal activity [*Gràcia et al*., 1998]. Dotted box corresponds to the area shown in Figure 2. See text for sources of multibeam bathymetry data.

2001]. Central volcanoes are distinct features that do not produce spatially continuous ribbons of overthickened volcanic crust away from the axis, indicating that the focusing of melt and eruptions are not continuous over time. Instead, a succession of central volcanoes rifted and with their flanks rafted off axis by seafloor spreading is clearly visible at the Lucky Strike area (Figure 1), suggesting a cyclic process instead. The present-day central volcano also displays a throughgoing narrow graben, corresponding to the initial rifting stages [*Humphris et al*., 2002]. Our understanding of this process is limited due to the lack of constraints on the mode of emplacement of central volcanoes along mid-ocean ridges (MORs), and on the onset and evolution of rifting leading to their dismemberment.

In this paper, we present a model for the emplacement and evolution of central volcanoes within the rift valley of slow and ultraslow spreading MORs based on near-bottom sidescan sonar data and seafloor observations from Lucky Strike, and a comparison to other sites along other slow spreading ridges. The Lucky Strike area has been intensively studied in recent years, and the regional, segment-scale setting [*Langmuir et al*., 1997; *Cannat et al*., 1999a; *Escartín et al*., 2001; *Gente et al*., 2003; *Ondreas et al*., 1997], and seismic crustal structure is well established [*Combier*, 2007; *Dusunur et al*., 2009; *Seher et al*., 2010a, 2010b, 2010c,

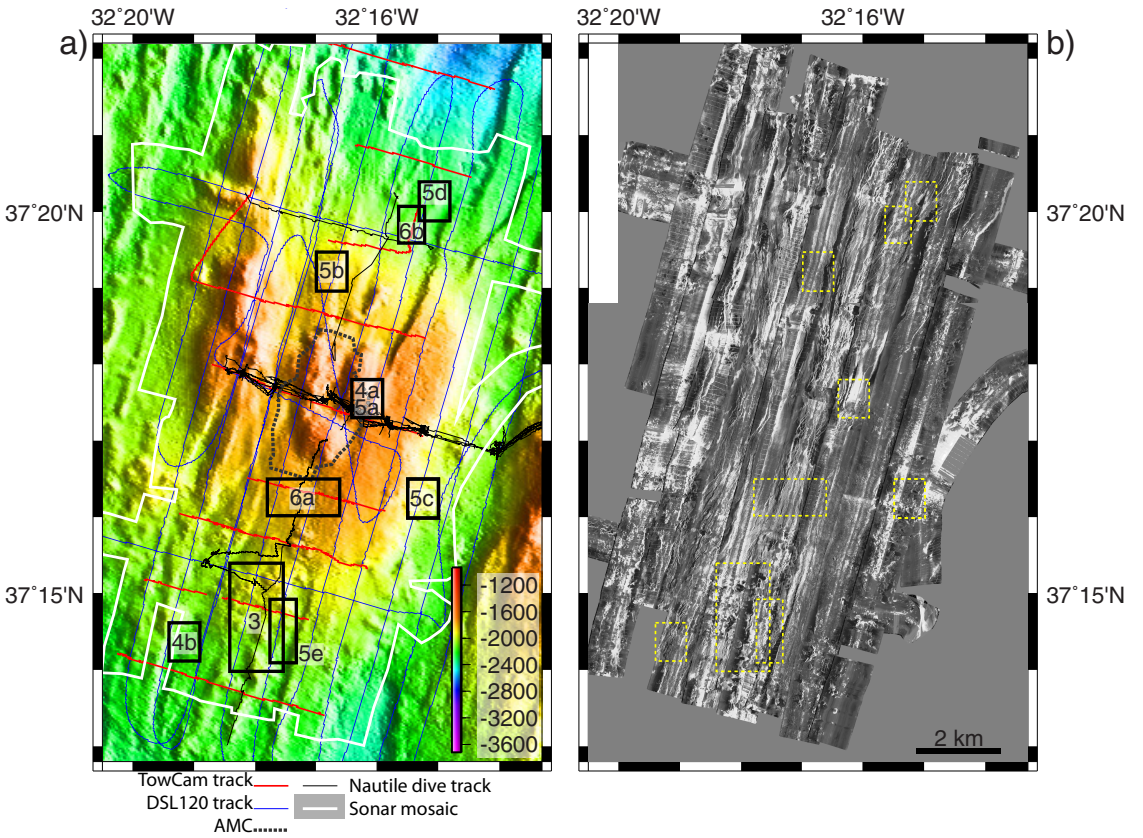

Figure 2. (a) Bathymetry of the Lucky Strike seamount, showing *TowCam*, *Nautile, and DSL120* tracks, and the outline of the final sonar mosaic. (b) West-looking sonar DSL120 sonar mosaic with a pixel resolution of ~3 × 4 m in *x* and *y* directions. The full-resolution West and East-looking sonar mosaics are provided in supporting information Figures 1a and 1b. Boxes in both Figures 2a and 2b and labels on Figure 2b indicate location of sonar images shown in Figures 4–6.

2010d; *Singh et al*., 2007]. These studies have been complemented by near-bottom, high-resolution sidescan sonar [*Humphris et al*., 2002; *Scheirer et al*., 2000], together with shipboard data [*Cannat et al*., 1999a, 1999b; *Escartín et al*., 2001], and limited visual ground truthing of the nature of the seafloor using deep-sea camera tows and submersible dives. With these data and their interpretation, we reconstruct the recent history of the Lucky Strike segment center, with the emplacement and ongoing rifting of the central volcano, while revealing the links between focused magma supply, volcanic activity, and tectonic extension within the rift valley floor. A systematic review of existing multibeam bathymetry along slow and ultraslow spreading ridges also reveals central volcanoes in different stages of rifting. Thus, the inferred history of central volcano emplacement and rifting for Lucky Strike may be applicable to similar features along the axis of the global MOR system.

2. Geological Setting

The ~70 km long Lucky Strike segment is located near the Azores hot spot and the triple junction between the North American, African, and Eurasian plates, and spreads at a present-day full rate of ~20–25 km/Myr [*Cande and Kent*, 1992; *Cannat et al*., 1999a; *DeMets et al*., 1990; *Escartín et al*., 2001; *Luis and Miranda*, 2008; *Luis et al*., 1994]. The Lucky Strike segment formed ~10 Ma after the rifting of an oceanic plateau associated with a magmatic pulse originating at the Azores hot spot [*Cannat et al*., 1999a; *Escartín et al*., 2001; *Gente et al*., 2003]. Seafloor formed since this breakup shows ridge-parallel, fault-bound abyssal hills (Figure 1). The rift valley displays a widening and a deepening of its floor (Figure 1), as well as a crustal thinning [*Detrick et al*., 1995; *Escartín et al*., 2001] toward the ends of the segment; all of these features are typical of linear, magmatic slow spreading ridge segments.

The Lucky Strike segment center hosts a prominent central volcano ~10 km in diameter and rising ~500 m above surrounding seafloor, emplaced within a ~20 km wide rift valley bounded by two large faults with

vertical throws of >500 m (Figures 1 and 2). The seamount summit displays three highs that surround a depression where recently lava was ponded and drain back [*Ondréas et al*., 2009]. Hydrothermal venting occurs at the edges of this depression and along the faults formed along the central graben [*Langmuir et al*., 1997; *Humphris et al*., 2002; *Ondréas et al*., 2009; *Ondreas et al*., 1997], which is the locus of recent volcanism and accretion [e.g., *Scheirer et al*., 2000; *Miranda et al*., 2005]. This hydrothermal field is one of the largest known to date, extending over ~1 km^2 [*Humphris et al*., 2002; *Ondréas et al*., 2009; *Barreyre et al*., 2012].

The central volcano is underlain by a ~3.5 km deep axial magma chamber (AMC) extending ~6 km along and ~4 km across axis [*Combier*, 2007; *Singh et al*., 2006]. Crustal thickness below Lucky Strike seamount is ~7.5 km, decreasing to 5.5 km at 15 km from the seamount summit toward the segment ends [*Seher et al*., 2010c; *Crawford et al*., 2010]. Seismic reflection data reveal fault planes cross-cutting the central volcano and restricted to the crust above the AMC, while the bounding faults penetrate to depths greater than the melt lens reflector [*Combier*, 2007]. In this area, seismic Layer 2A is anomalously thick and displays low seismic velocities, consistent with emplacement of a ~700–900 m thick sequence of extrusives [*Arnulf et al*., 2014]. The AMC is underlain by a low-velocity zone [*Seher et al*., 2010c], which may correspond to a melt-rich region at lower crustal levels. A microseismic experiment conducted in the area showed events extending to a depth of ~6 km and around the AMC, and sustained activity above the AMC and along the axial graben, likely due to hydrothermal circulation and cooling along axis [*Dusunur et al*., 2009; *Crawford et al*., 2013]. This area experienced a seismic event in 2001 recorded by moored hydrophones, with a hydroacoustic signature suggesting a magmatic (diking) trigger with no known volcanic expression at the seafloor [*Dziak et al*., 2004].

3. Data Acquisition, Processing, and Analysis

Data sets used in this study include shipboard multibeam bathymetry, near-bottom sidescan sonar backscatter imagery, and near-bottom magnetics. The base multibeam bathymetry data (Figures 1 and 2) were acquired during the Sudaçores [*Cannat et al*., 1999a; *Escartín et al*., 2001]. Higher-resolution shipboard bathymetry was also acquired during the Flores'97 (PI Y. Fouquet) and Sismomar'05 (PIs S. Singh and W. Crawford) cruises, and complemented with bathymetry data publicly available through Marine Geoscience Data System (http://www.marine-geo.org). Sidescan sonar data were acquired with the deep-towed 120 kHz system DSL120 (WHOI) during the Lustre'96 cruise [*Humphris et al*., 2002; *Scheirer et al*., 2000]. The sonar survey (Figure 2) was carried out at an altitude of ~100 m above the seafloor, and navigated with an acoustic long baseline transponder network that provided a precision of ~20 m or better in vehicle location. Most tracks were run subparallel to the ridge axis and spaced ~800 m apart, with additional across-axis tracks for navigation control. The survey insonified 120 km^2 of seafloor extending ~10 km across and ~16 km along axis (Figure 2). Additional details on sonar characteristics, cruise plan, data acquisition, and prior data processing are available elsewhere [*Scheirer et al*., 2000]. A three-component magnetometer was installed on the deep-tow DSL120 system during surveys. The derived seafloor magnetization, presented in *Tivey and Dyment* [2010, Figure 4], indicates that the survey area is within the central magnetic anomaly (i.e., <0.7 Myr).

Complementing the bathymetry and sidescan data, visual seafloor observations were carried out during the Graviluck'06 cruise (PI V. Ballu) using both the IFREMER *Nautile* submersible and the WHOI deep-towed *TowCam* camera system [*Fornari*, 2003]. *Nautile* dives were run both along axis and extending off axis from the Lucky Strike hydrothermal field to the bounding wall. A total of 10 *TowCam* profiles were carried out, primarily across axis (Figure 2). We generated georeferenced mosaics from *TowCam* images and navigation to facilitate visual seafloor characterization [*Escartín et al*., 2008a; *Prados et al*., 2012].

3.1. Sonar Processing and Generation of Mosaics

DSL120 sidescan sonar data have a nominal ~0.5 m across-track resolution while surveying ~100 m above seafloor, and at this altitude, sonar penetration in sediment [*Mitchell*, 1993] is very limited (<1–2 m). As the Lustre'96 data were originally processed at a resolution of 10 m [*Humphris et al*., 2002; *Scheirer et al*., 2000], we reprocessed the raw sonar data at a resolution of ~3 and 4 m in the along and across-track directions, respectively. These higher-resolution sonar images (available at http://www.marine-geo.org) allow us to better exploit the acoustic backscatter data and identify tectonic and volcanic features. The sonar survey of the

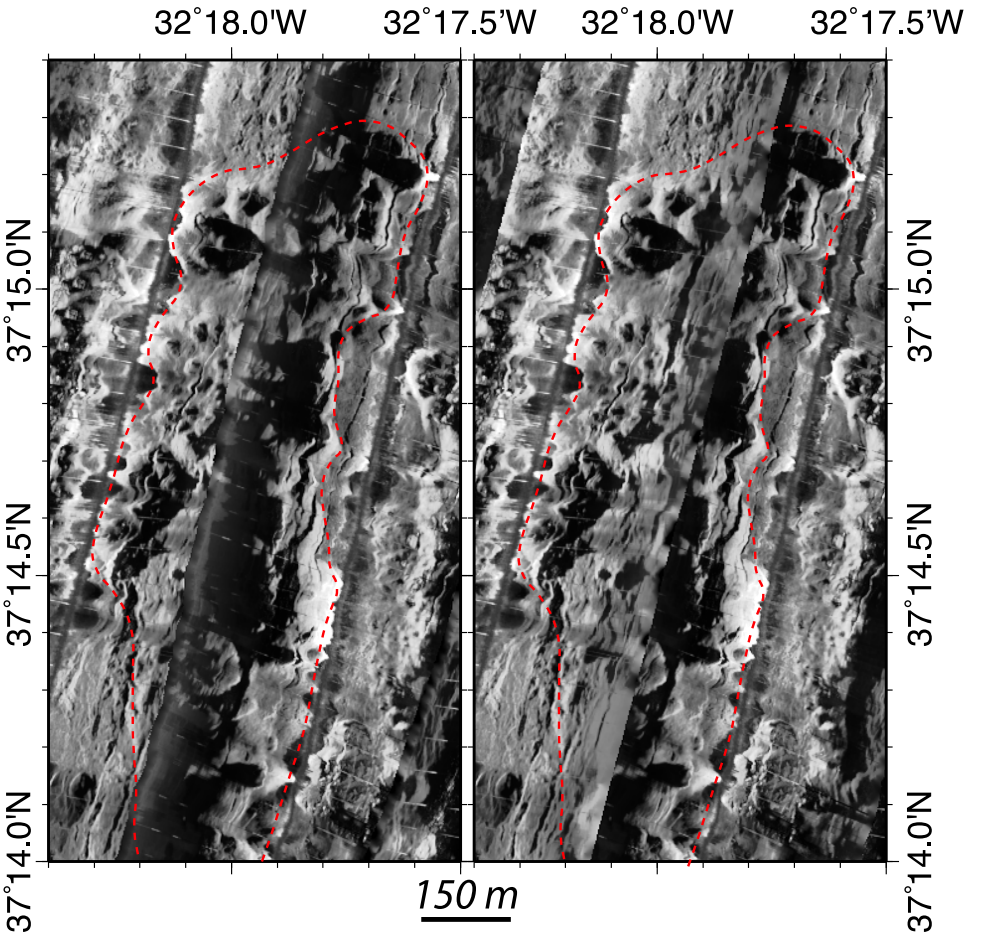

Figure 3. Acoustic backscatter maps of an axial volcanic ridge (outlined by dashed red line) with (left) westward and (right) eastward insonification directions. Notice the west flank of the volcanic ridge masked by acoustic shadows in the westward mosaic, while the eastward mosaic properly insonifies it, showing its texture and crosscutting faults.

rift valley floor extends ~15 km along axis, and off axis to 3–4 km (spreading age of ~300–400 kyr, Figures 2 and 3). To facilitate the geological interpretation of acoustic backscatter data, we generated two sonar mosaics, with westward (Figure 2b) and eastward overlap of adjacent tracks (full-resolution mosaics in supporting information Figures 1a and 1b). The two mosaics allow us to visualize zones masked by adjacent and overlapping sonar swaths or in acoustic shadows, providing eastward and westward insonification directions. Complementary insonification directions, where available (e.g., Figure 3), facilitate the volcanic and tectonic interpretation of the sonar data [*Escartín et al*., 1999; *Searle et al*., 2010].

3.2. Sonar Interpretation

In our sonar interpretation, we identify tectonic features (faults and fissures, Figure 4, available at http://www.marine-geo.org), acoustic backscatter facies (Figure 5), and primary volcanic features (Figure 6). Volcanic interpretation of sonar textures is similar to that proposed for TOBI sonar data elsewhere along the Mid-Atlantic Ridge [*Smith and Cann*, 1993; *Smith et al*., 1995a], but adapted to the higher resolution of the DSL-120 data. Imagery from *TowCam* and *Nautile* (Graviluck'06 cruise) provides visual constraints on the types of lava morphologies associated with these volcanic units (Figure 7). From these interpretations, we determine the geometry and distribution of volcanic units and tectonic features throughout the area (Figures 8 and 9) that reflect the volcanic and tectonic history of the area (Figure 10).

3.2.1. Faults and Fissures

Sonar data were used to map the trace of fissures and faults (Figure 4) and to determine the fault dip direction. Digitized faults traces correspond to the top of the fault scarp (Figures 4a and 4c), which can be clearly identified regardless of insonification direction. The limited overlap of adjacent swaths does not allow us to

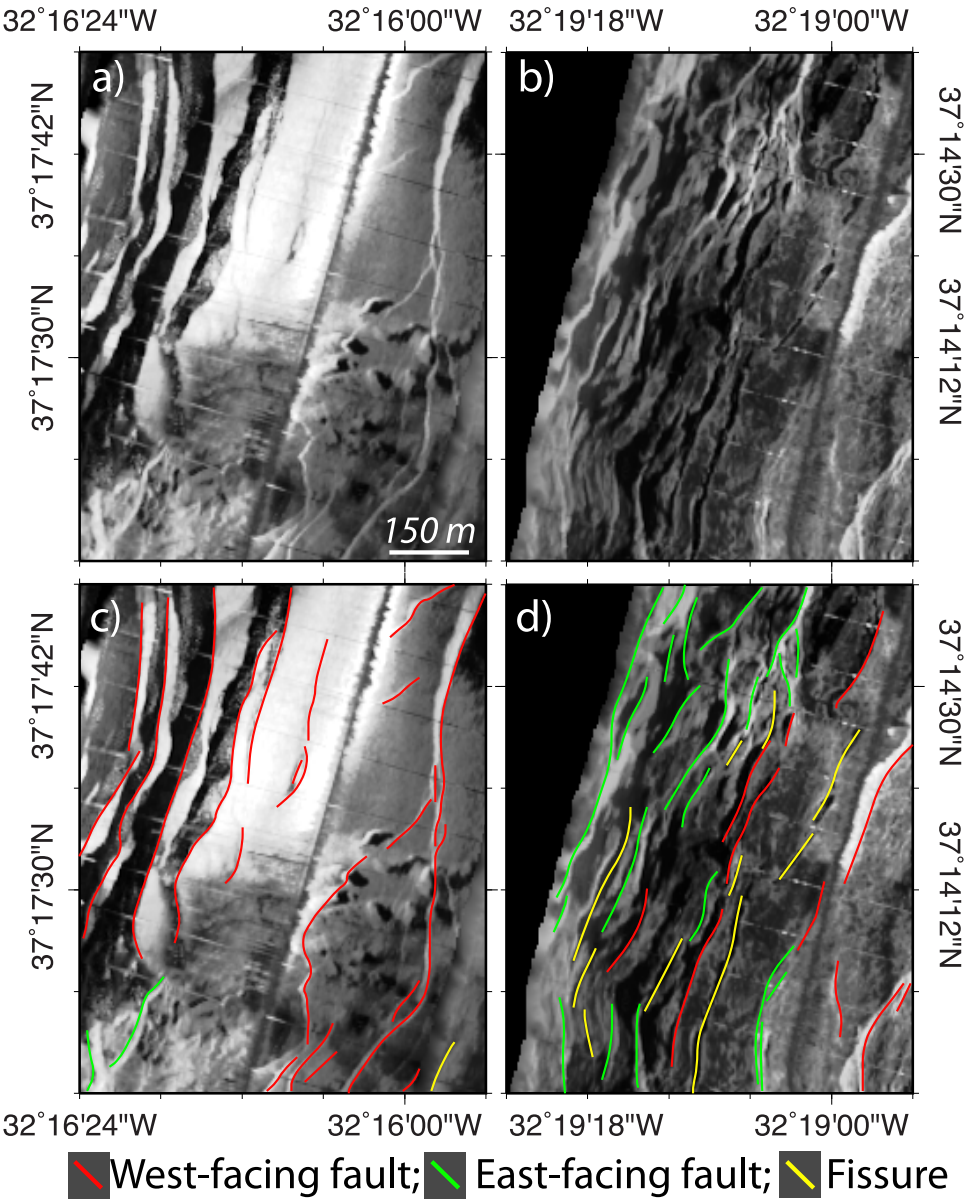

Figure 4. Examples of (a and b) sonar images and (c and d) corresponding interpretation of faults and fissures. Fault scarps are clearly visible either as shadow zones (Figure 4a, top left) or as bright acoustic reflectors (Figure 4a, right), depending on insonification direction. We digitize scarp tops as they can be clearly identified whether scarps are acoustically illuminated or in shadow (Figure 4c). Complex set of fissures and faults dissecting a volcanic ridge (Figure 4b). Fissures are characterized by a narrow, linear shadow zone, and are often associated with small-scale faulting (Figure 4d).

quantify fault scarp width in plan view, which may be a proxy for fault scarp height [e.g., *Escartín et al.*, 2007; *MacLeod et al.*, 2009].

Fissures are linear structures, with no apparent or significant scarp relief, that show edges flanking a shadow zone corresponding to the fissure gap (Figures 4b and 4d). We also attributed clear alignments of elongated seafloor collapses to fissures, which are probably arrested before breaching the seafloor. These data cannot be used to determine the width of individual fissures, necessary to quantify extension associated with these tensional cracks. Figure 8a shows the fault and fissure map throughout the study area.

3.2.2. Acoustic Seafloor Texture

After accounting for the effects of insonification direction and local seafloor slopes, seafloor acoustic texture reflects primarily the mode of volcanic accretion, nature of seafloor deformation (faults, fissures), or mass

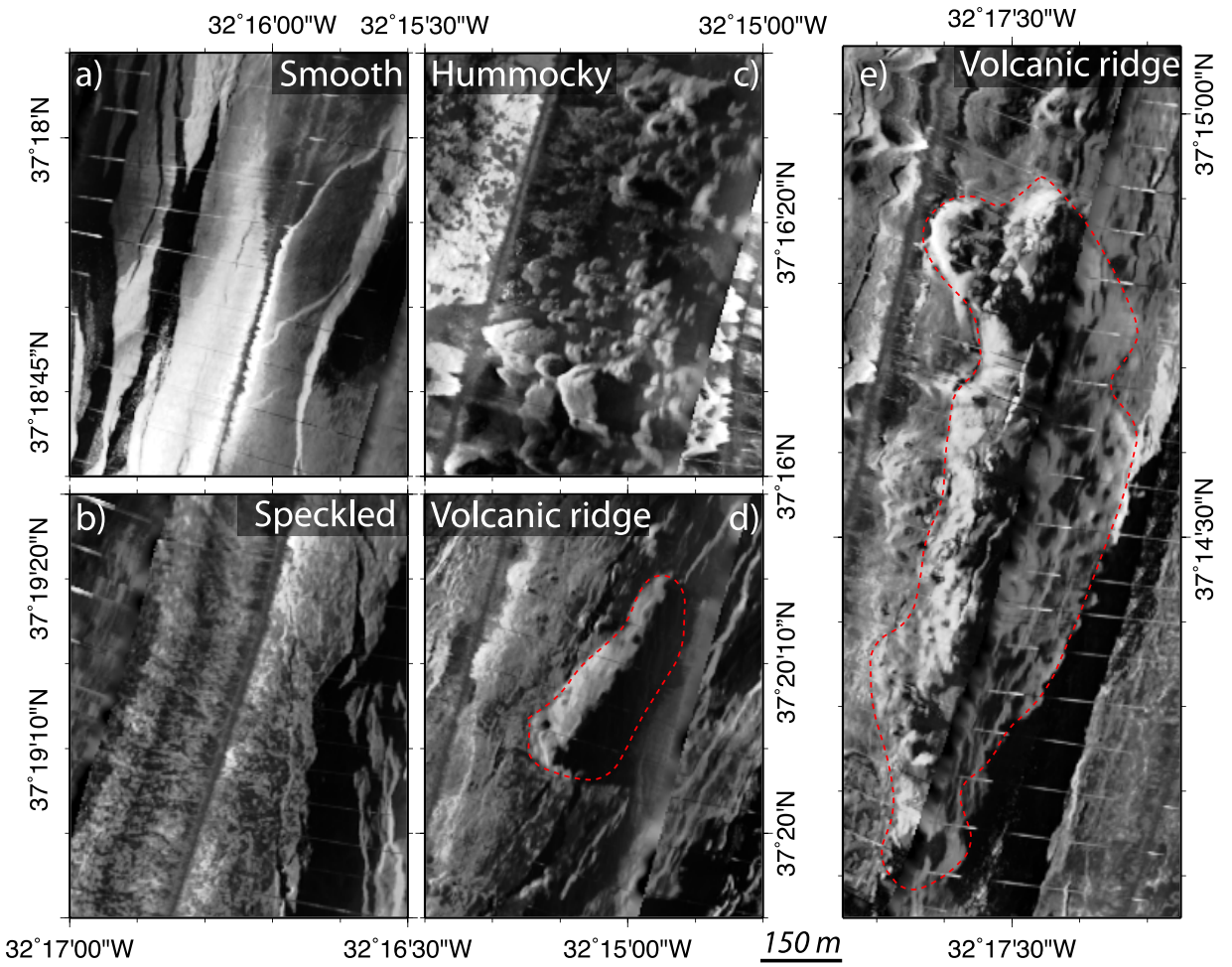

Figure 5. Examples of acoustic facies identified in the sidescan sonar mosaics. (a) *Smooth terrain* is featureless. (b) The *speckled terrain* shows a texture with reflective (white) and nonreflective (dark) patches with a characteristic size of ~10 m or less, and no significant relief. (c) *Hummocky terrain* corresponds to a bulbous texture associated with small-scale mounds (10–100 m diameter in plan view), with their vertical relief indicated by the acoustic shadows. (d and e) *Volcanic ridges* are well defined, continuous, and elongated structures that extend along axis several hundreds of meters, and have reliefs of tens of m.

wasting (collapses), in addition to sedimentation [e.g., *Blondel*, 2009]. The Lucky Strike volcano displays large areas that are relatively unfaulted, and the primary (volcanic) seafloor texture is readily identifiable throughout the survey area. In deformed terrain, the original seafloor texture is preserved on the surface of fault-bound seafloor blocks.

We have identified four distinct acoustic facies that are independent of backscatter intensity: Smooth terrain, speckled terrain, hummocky terrain, and volcanic ridges (Figure 5), in addition to recent lava flows (Figure 6), and correlated these to available seafloor imagery (Figures 2 and 7). The lateral transition between facies is often poorly defined or gradual, and thus, these represent end-member facies. To construct the acoustic facies map shown in Figure 8b, we accounted for zones where transitions are not sharp, or where two or more textures are present at small spatial scales. In these cases, the seafloor is assigned to the dominant facies over an area of ~200 m × 200 m.

Smooth Terrain. Smooth acoustic facies on Lucky Strike seamount shows a homogeneous backscatter without recognizable features (Figure 5a). Areas of smooth terrain are present throughout the sonar survey area, but occur dominantly at the volcano summit of the volcano, surrounding the three highs. Similar textures reported from other MAR segments are interpreted as volcanic flows with very low relief and hence no acoustic shadows [*Cann and Smith*, 2005; *Searle et al*., 2010]. This acoustic texture is also reported at the center of a segment along the slow spreading Mariana back-arc basin [*Deschamps et al*., 2005]. In young seafloor, near the accretion zone and at the volcano summit, we observe locally fractured basalt sheet flows lightly sedimented (Figure 7a).

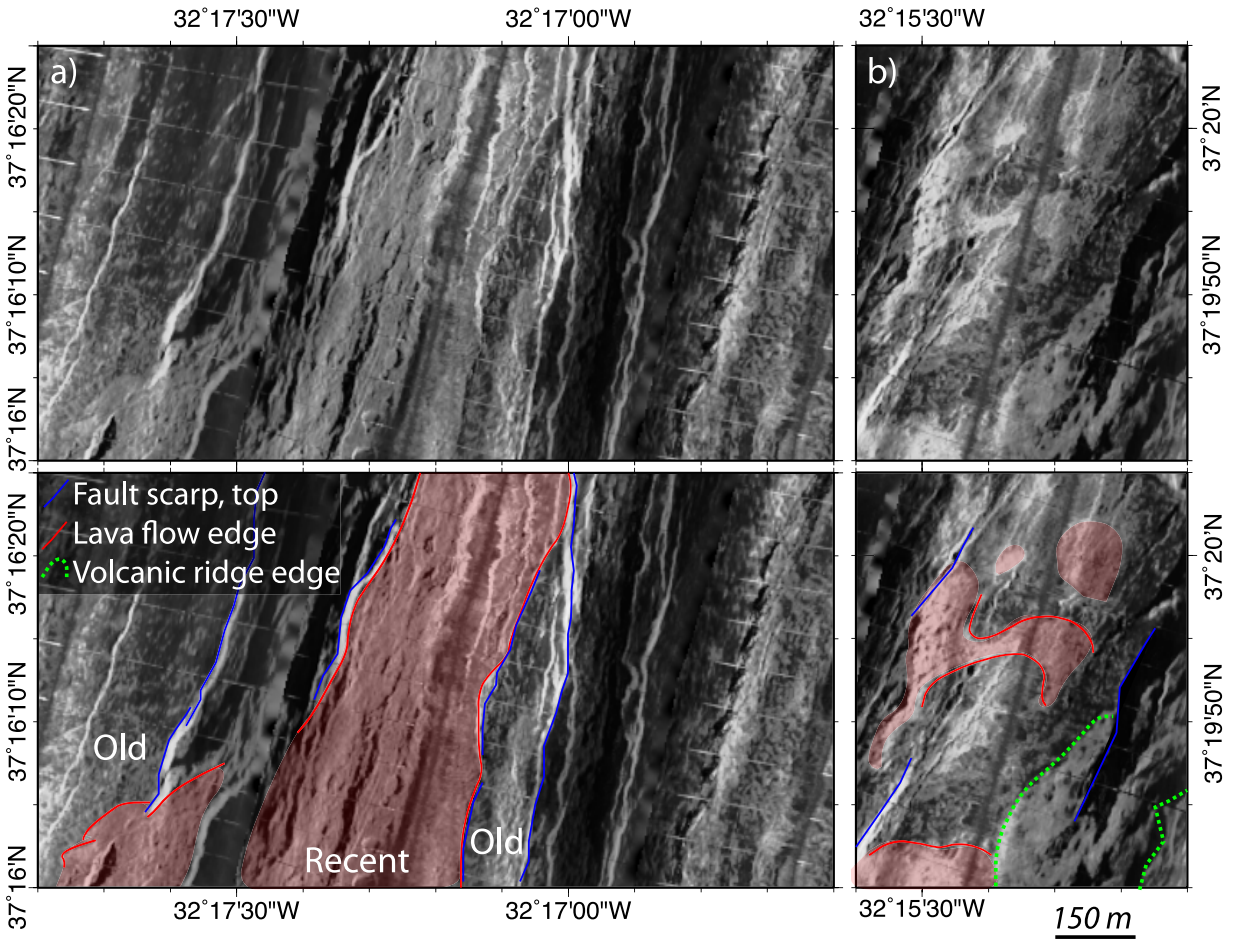

Figure 6. Sidescan sonar images of the neo-volcanic zone. (a) Near the volcano summit, the axial graben floor is covered with recent lava flows (higher acoustic backscatter) than the older, sedimented seafloor beyond the bounding fault scarps. Flows extend away from the graben and over sedimented floor in the southwest portion of the image. (b) Recent lava flows emplaced over older, sedimented seafloor. The limits of volcanic ridges (green dashed line) and fault scarps (blue) are also shown.

In these areas, the underlying flows are likely to be smooth, as rocks outcropping through otherwise sedimented terrain, as deduced from the *Nautile* and *TowCam* observations, suggest a very thin sediment layer. Away from the segment center, at the margins of the rift valley floor near the edges of the sonar survey, this acoustic facies corresponds instead to sedimented seafloor, and where the original volcanic texture is completely buried. Sediments include mass-wasted debris shed from the mid to lower rift walls, with debris trails at the base of scarps, well imaged in the sidescan data [*Scheirer et al*., 2000].

Speckled Terrain. This acoustic facies is characterized by variations from high to low acoustic backscatter at small spatial scales of 5–25 m, often displaying a weak elongation with consistent directions over wide areas (Figure 5b). This facies is also found throughout the study area, but tends to define a continuous concentric belt around the smooth terrain on the flanks of the central volcano (Figure 8b). Seafloor imagery shows that this texture is associated primarily with hackly sheet lava flows (Figure 7c), and locally to pillow and lobate lavas, with small ponds of sediment throughout (Figures 7b and 7c).

Hummocky Terrain. This acoustic facies is characterized by the juxtaposition of numerous circular or elliptical mounds, with diameters ranging from ~10 to ~100 m (Figure 5c). This acoustic facies, although present throughout, is found primarily at the edges of the survey area, and is often associated with volcanic ridges (see below and Figures 5d and 5e). Similar terrain is commonly observed along the rift valley floor of the MAR [*Briais et al*., 2000; *Lawson et al*., 1996; *MacLeod et al*., 2009; *Smith et al*., 1995a; *Smith et al*., 1995b], and along the Southwest Indian Ridge (SWIR) [*Sauter et al*., 2002]. Each hummock may be an individual volcanic cone, according to near-bottom multibeam bathymetry of the MAR axis at 45°N [*Searle et al*., 2010]. In these areas, the seafloor is paved almost exclusively by pillow lavas elongated in a direction that conforms to local slope (Figure 7d).

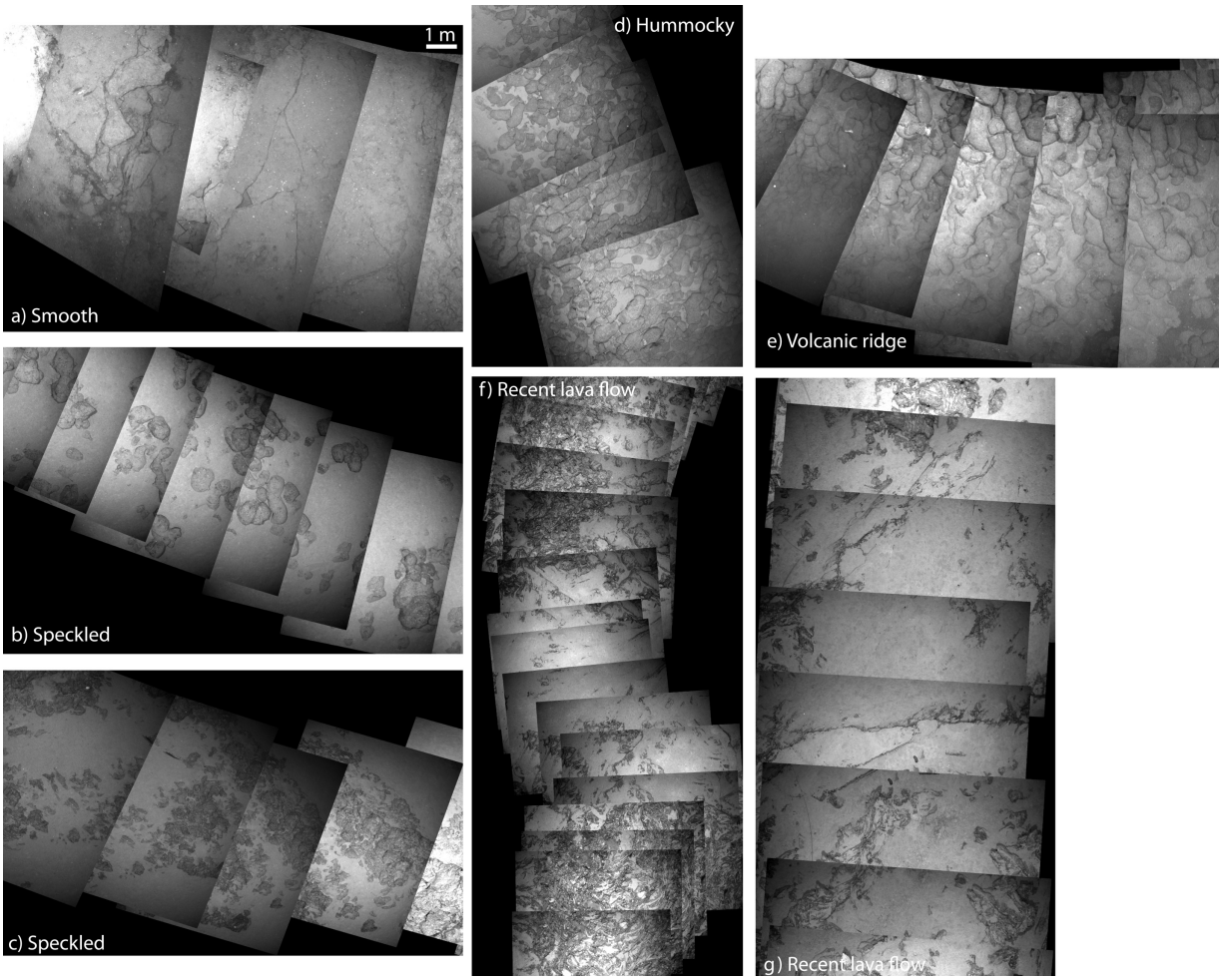

Figure 7. Seafloor images acquired with the *TowCam* (see Figure 2) over different acoustic facies: (a) sedimented sheetflows on smooth terrain; (b) sedimented pillows and (c) lava flows on speckled terrain; (d) pillows on hummocky terrain; (e) pillow lavas on the flank of a volcanic ridge; (f and g) recent lava flows. All images are at the same scale (see Figure 7a).

Volcanic Ridges. Sidescan data shows continuous and elongated structures, in general, subparallel to the ridge axis trend, with lengths of ~100 m to more than ~4 km. Available shipboard multibeam bathymetric data reveal the largest features, which have relief of more than 100 m, generally display well-defined limits, and correspond to both smooth and hummocky textures (Figures 6d and 6e). Cross-cutting relationships suggest that these volcanic ridges are emplaced over the surrounding seafloor, and result from localized fissure eruptions [*Head et al*., 1996; *Smith et al*., 1995b]. Similar structures are identified along the axis of other MORs [*Mendel et al*., 2003]. Based on the intensity of deformation (density of faults and fissures), we have distinguished between unfaulted (Figures 5d and 5e) and faulted volcanic ridges (Figure 3). The seafloor at volcanic ridges is similar to that found in hummocky terrain, with elongated pillow lavas indicating downslope flow (Figure 7e).

3.2.3. Individual Eruptive Units

To supplement the seafloor acoustic texture interpretation, we delineated individual eruptive units where possible. Flow contacts identified along *TowCam* image tracks based on changes in sediment cover and morphology were correlated to backscatter variations in sonar data. Coherent acoustic features were then interpolated away from *TowCam* tracks, and a relative age and dominant morphology were assigned to each identifiable flow unit.

The least ambiguous volcanic features identified using these methods are young lava flows. The flows have high acoustic backscatter resulting from their relief and an absent or thin sediment cover (<1 m) that is acoustically transparent. These flows correspond to recent eruptions paving over the surrounding older, sedimented

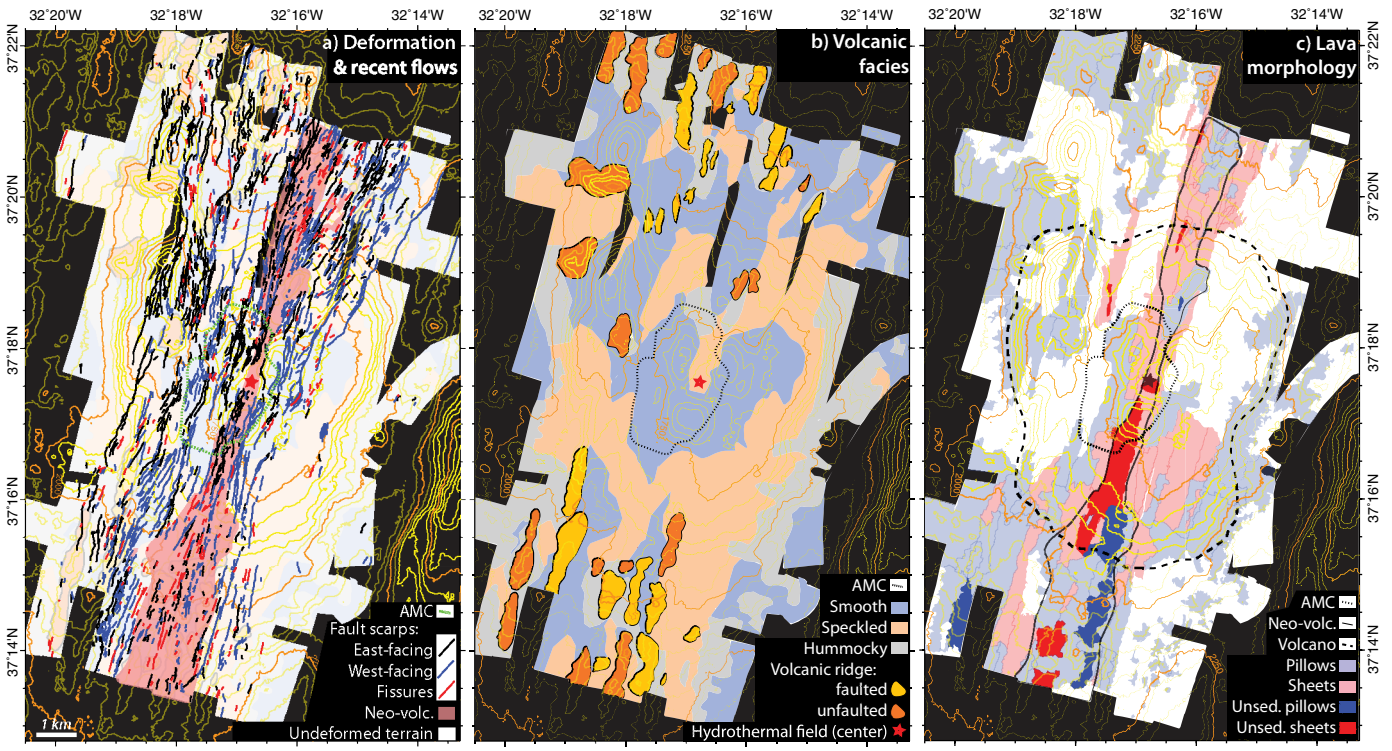

Figure 8. (a) Fault and fissure map, including fault orientation and mapping of the axial neo-volcanic zone. (b) Interpretation of acoustic volcanic facies (smooth, speckled, and hummocky terrain, faulted and unfaulted volcanic ridges). Note that the volcanic ridges appear within 2–3 km of the volcano summit where the hydrothermal field is found (red star). (c) Mapped eruptive units and their dominant morphology (pillow or sheet). The extent of the volcano is defined from a break in slope at the volcano base and should be considered approximate, and is used to determine the relative proportion of sheets to pillows on and off the seamount. The outline of the axial magma chamber (AMC) [*Combier*, 2007] and the position of the hydrothermal field is indicated in all maps.

seafloor (Figure 6), as supported by the lack of faults and fissures. Seafloor observations (camera tow, submersible) also demonstrate that these lava flows have the youngest appearance visually, and exhibit a thin sediment cover.

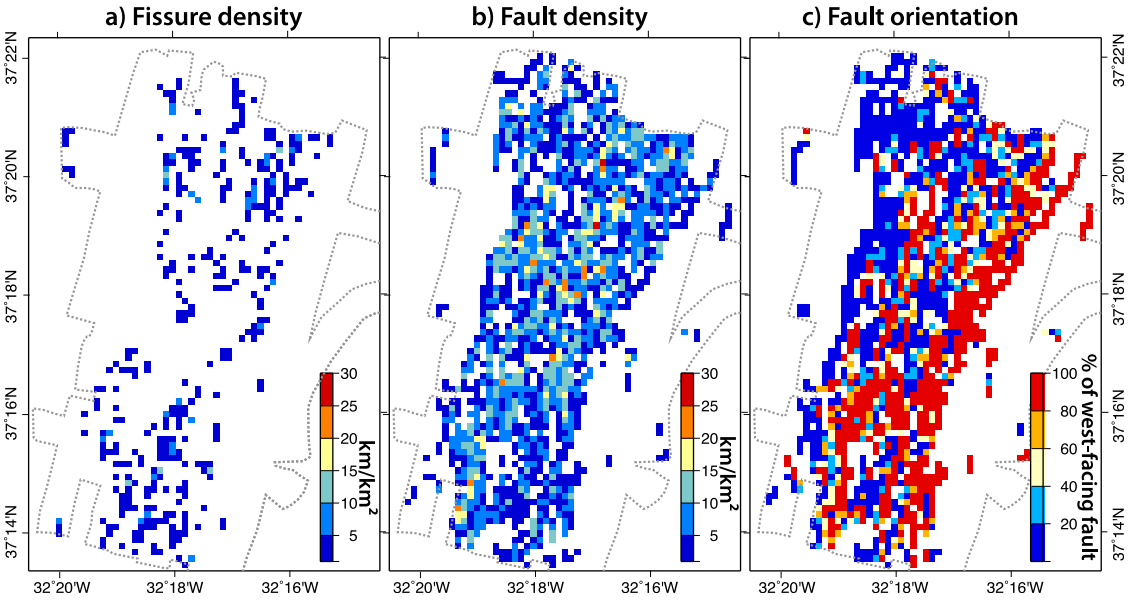

Figure 9. Spatial variations in (a) fissure density, (b) fault density, and (c) fault orientation throughout the study area. Volcano flanks are unfaulted (white zones on E and W of the surveyed area). Away from the volcano summit, faults do not show a well-defined axis toward which faults dip, and instead both east and west facing are distributed throughout the rift valley floor.

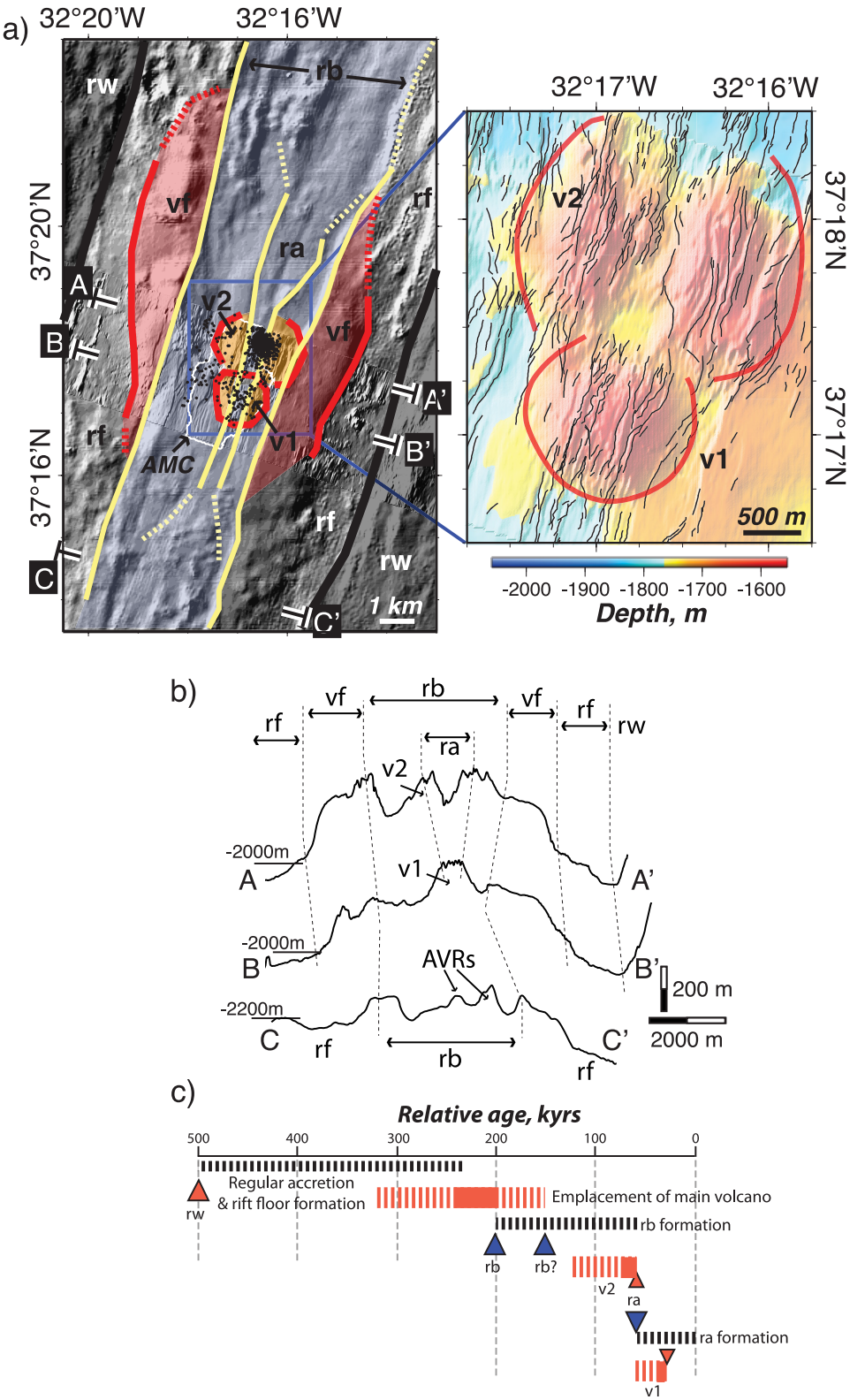

Figure 10. (a) Structural interpretation of the Lucky Strike central volcano (left) and close-up of the rifted volcanoes at the summit of the Lucky Strike seamont (right) showing the digitized faults and fissures (Figure 8). The structural map shows the main rift valley walls (*rw*) and rift valley floor (*rf*), the unfaulted volcano flanks (*vf*) emplaced within it, the two successive axial grabens dissected the volcano (*rb* and *ra)*. Graben *ra* has dissected two summit volcanic cones (*v1 and v2*). Note that the most recent graben has a limited along-axis extension. (b) Across-axis sections showing the along-axis structural variations from the volcano summit and across the two volcanic cones *v2* and *v1* (*A-A'* and *B-B'*, respectively), and cross the rift valley away from the summit (*C-C'*). (c) Temporal evolution of the different volcanic and rifting events in the Lucky Strike area. Dashed lines indicate the time span of volcanic emplacement based on spreading age, and the shorter solid bar illustrates a more probable, faster volcanic emplacement (see text for details).

Lava flow edges can be controlled by fault scarps acting as topographic barriers arresting the flow, as observed along the graben immediately south of the hydrothermal field (Figure 6a). In other areas, recent lava flows that are not restricted topographically show instead curved edges that result from downslope transport and emplacement of lava over sedimented seafloor (Figure 6b). Lava flow advance can also be obstructed at the flanks of preexisting volcanic ridges (Figure 6b). Similar lava flow age differences and associated variations in acoustic backscatter have been identified in sonar surveys along the East-Pacific Rise [*Fornari et al*., 2004]. At that location, recent lava flows sourcing at the axial summit trough and repaving the adjacent seafloor show edges controlled by topographic barriers such as inward-facing fault scarps [*Fornari et al*., 2004, 2012; *Escartín et al*., 2007; *Soule et al*., 2009].

Seafloor imagery at Lucky Strike documents a complex volcanic structure, with sheet, ropy, and jumbled lava textures (Figures 7f and 7g). The relatively young age inferred from the high-backscatter areas corresponds to either unsedimented lava flows (e.g., at the center of the Lucky Strike hydrothermal field) [*Humphris et al*., 2002; *Ondréas et al*., 2009], or to areas where light sedimentation allows visual identification of lava structures (Figures 7f and 7g).

4. Results

Figure 8 shows the traces faults and fissures dissecting the Lucky Strike central volcano (Figure 8a), the distribution of acoustic facies in the study area attributed to volcanic features (Figure 8b), and the identified eruptive units and their dominant morphology (Figure 8c).

4.1. Distribution and Quantification of Deformation

Figure 8a shows east and westward-facing fault traces and fissure traces, extending over a zone 6–8 km wide in the across-axis direction. Some of the faults accumulate strain efficiently, and develop as larger faults that bound grabens, such as the recent graben developed within this deformed zone, and that dissects the central volcano. It is well defined at its summit, with a width of ∼0.7 km, and bound by inward-facing faults. At this location, the axial graben dissects two preexisting volcanic cones (Figure 10a). The northern one has been fully dismembered and split by the axial graben, identifiable in shipboard bathymetric data. The southern volcanic cone, instead, is cut by an incipient graben hosting a dense network of faults, and owing to its low relief it is not identifiable in shipboard bathymetry. This axial graben shows a local bathymetric low infilled by ponded lava flows that drained back into eruptive vents [*Scheirer et al*., 2000; *Humphris et al*., 2002; *Ondréas et al*., 2009; *Barreyre et al*., 2012]. Hydrothermal activity is concentrated around this bathymetric depression, and preferentially along the faults forming the graben walls [*Ondréas et al*., 2009; *Barreyre et al*., 2012].

The axial graben widens toward the north and south away from the volcano summit, and is poorly defined within a few kilometers of the segment center. This widening is achieved by faults developing oblique to the overall segment trend, fanning away from the ridge axis at angles that can reach locally $>30^\circ$ with respect to the overall 010–015° ridge trend (Figure 8a). This fault pattern imparts an hourglass shape to the axial graben; a similar tectonic structure is reported at the center of the 17°N segment along the Mariana back-arc basin [*Asada et al*., 2007]. Faulting is distributed throughout these wider sections of the axial graben, with faults facing in both directions, and with no clearly defined zone of most recent deformation or accretion as visible in the fault trace (Figure 8a) and orientation maps (Figure 9c). Away from the volcano summit, we also observe a widening of both the zone of recent volcanism (from <1 km at the summit to >3 km away from it, Figure 8b) and of the faulted and fissured zone (widening to 5 and 8 km to the south and north, respectively, Figures 9b and 10b).

The sidescan data also document variable deformation, with ∼60% of the surveyed crust showing faults (∼70 km^2 out of 120 km^2). The remaining ∼40% of the seafloor displays no apparent seafloor deformation, and corresponds primarily to the western and eastern flanks of the volcano (Figures 9a and 10). We observe no relationship between distance to the axis and intensity of deformation, demonstrating that the fissure and fault density are not a proxy for seafloor age. This heterogeneity in deformation is clear in the fault density map (Figure 9b), where local fault densities can reach values >20 km/km^2, compared to an average density of ∼3.5 km/km^2 for the survey area (Table 1). Fissuring is systematically associated with faulted areas, and better developed away from the volcano summit (Figure 9a), yielding a fissure density of

Table 1. Summary of Intensity of Deformation Inferred From High-Resolution Sonar Surveys for Lucky Strike (This Study) and Other Mid-Ocean Ridge Sections With Similar Sonar Data Available

		Faults		
	Fissures	W Facing	E Facing	All
MAR at Lucky Strike, ~22 km/Myr (This Study)				
Density (survey area)[a], km/km^2	0.39	1.59	1.87	3.47
Density (deformation zone)[b], km/km^2	0.67	2.77	3.26	6.03
MAR at TAG, ~24 km/Myr [Bohnenstiehl and Kleinrock, 1999]				
Density (survey area)[c], km/km^2				0.96
Mariana Back-Arc Basin at 17°N, ~33 km/Myr [Asada et al., 2007]				
Density (survey area)[d], km/km^2	0.93			3.97
Density (survey area)[e], km/km^2	1.98			2.98
Mariana Back-Arc Basin at 18°N ~33 km/Myr [Asada et al., 2007]				
Density (survey area)[d], km/km^2				1.48[f]
Galapagos Spreading Center at 90°W −92.5°W ~52–55 km/Myr [Mittelstaedt et al., 2012]				
Density (survey area)[d], km/km^2				0.22
EPR at 9°25′N–58′N, ~110 km/Myr [Escartín et al., 2007[g]				
Density, AST, km/km^2	3.49			4.24
Density, "young" crust, km/km^2	0.40			0.59
Density, "old" crust, km/km^2	2.05			2.77
Density, survey area, km/km^2	0.80			1.12
EPR at 9°N Overlapping Spreading Center, ~110 km/Myr [Klein et al., 2013] [h]				
Density, all survey area, km/km^2				3.04[f]
Density, fissured axial area, km/km^2				7.08[f]

[a]Cumulative fissure or fault length (km) per surface of SDL120 sonar survey (119.6 km^2).
[b]Cumulative fissure or fault length (km) per surface of seafloor showing deformation (fissured or faulted, 68.7 km^2).
[c]Cumulative fissure or fault length (km) per surface interpreted sonar survey surface (94.5 km^2). Fault length has been calculated after digitization of fault traces in *Bohnenstiehl and Kleinrock* [1999, Figure 4], and the survey surface shown in this same Figure 4.
[d]Cumulative fissure and fault length (km) per sonar survey surface (200 km^2 for 17°N and 100 km^2 for 18°N). Fault length has been calculated from the total length of both faults and fissures at 17°N (794 and 187 km, respectively, M. Asada, personal communication, 2013). For 18°N, the total number tectonic features (462) and the average length (320 m) of both faults and fissures combined is reported instead [*Asada et al*., 2007].
[e]Cumulative fissure and fault length (km) per sonar survey surface (200 km^2). Fissure and fault length have been calculated from their average length (118 and 335 m, respectively) and the number of features (2347 and 1777, respectively) as reported by [*Asada et al*., 2007; *Deschamps et al*., 2005].
[f]Reported density corresponds to the combination of both faults and fissures.
[g]Fault and fissure parameters are extracted from an equivalent dataset acquired with the same sonar system, and therefore of comparable quality and resolution.
[h]Combined fissure and fault density from *Klein et al*., [2013] published maps, provided by S. White (personal communication, 2014), with no distinction between faults and fissure densities.

~0.4 km/km^2, which is an order of magnitude lower than the density of faults (Table 1; Figure 9a). The average fault density we report at the deformed area of Lucky Strike is significantly higher that from other sites for which similar near-bottom sonar-based studies are available (see Table 1 and references therein), while the fissuring density is relatively low.

4.2. Distribution of Volcanic Units

Identification and mapping of sonar acoustic facies throughout the survey area reveal the volcanic structure of Lucky Strike seamount (Figure 8b). The volcano summit shows a concentric band of smooth terrain ~2 km in radius around the hydrothermal field, which transitions radially to speckled terrain. This transition is best observed at the east and west seamount flanks where the volcanic structure is well preserved in the unfaulted terrane. Seafloor observations show that these areas are flat-lying lava flows, with moderate sediment cover.

The radially symmetric distribution of volcanic deposits is disrupted by an axial graben that cuts the seamount, as described above. The floor of the graben is paved with young, highly reflective lava flows with light sediment cover. We refer to this region as the neo-volcanic zone (Figures 9a and 9b). These flows are dominantly sheet flows that are confined within the axial graben by the bounding faults. Lava flows are absent on the seamount summit outside of the axial graben. The graben also coincides with the zone of highest magnetization [*Tivey and Dyment*, 2010], is underlain by microseismic activity [*Crawford et al*., 2013], and hosts the hydrothermal activity. All these characteristics clearly indicate that this is the locus of recent volcanic accretion and tectonic activity.

Elongated axial volcanic ridges (AVRs) are emplaced throughout the Lucky Strike rift valley floor at distances of >4 km along axis from the volcano summit, at the northern and southern edges of the survey area, where they cover a significant portion of the seafloor (Figure 8b). Their length varies between few hundred meters and up to ~4 km, and their typical width is ~100–300 m. Sidescan images reveal that they are variably faulted and/or fissured (Figure 8b), and that there is no systematic relationship between degree of deformation and distance to the present-day accretion axis. Both faulted and unfaulted AVRs are present across the surveyed rift valley floor (Figure 8b). This observation, together with the lack of a relationship between fault densitity and distance to the axis, suggests that degree of faulting is not a proxy for relative age of these structures. This is supported by seafloor observations at different AVRs, which show no apparent correlation between faulting density and sediment cover. Only one AVR showed little to no sediment cover, southwest of the survey area (~37°15′N, 32°20′W, Figure 8b), suggesting that volcanism may occur beyond the bounds of the seamount and outside of the active axial graben. The majority of the AVRs are elongated and subparallel to the overall ridge orientation, with the exception of smaller structures that are emplaced with an obliquity of 15°–20° with respect to spreading direction (e.g., at 37°19′N and 37°20.5′N, at the northwest margin of the survey area), and subparallel to faults fanning away from the volcano summit.

Hummocky terrain is associated with AVRs in the sidescan data. Pillow lavas also make up most of the rift valley floor between the edge of the central volcano and the rift bounding faults (Figure 8b). Hummocks likely dominate rift valley floor morphology prior to the emplacement of the central volcano, as observed along other slow and ultraslow spreading ridge sections [*Asada et al*., 2007; *Gomez et al*., 2006; *Searle et al*., 2010; *Smith et al*., 1999]. The smooth acoustic textures along the base of the rift valley wall scarps east and west of the survey area (Figure 8c) likely correspond to heavily sedimented terrain and mass wasting deposits burying basement structures.

5. Discussion

The limits of the Lucky Strike seamount, the width of the recent graben dissecting it, and the location of the two recent, variably faulted volcanic cones at the volcano summit allow us to constrain the history of volcanic emplacement and rifting of the seamount, and ultimately provide broad bounds to eruption rates in this area (section 5.1). These data also allow us to document along-axis changes in accretion style at the present time along the Lucky Strike segment center. These variations in accretion are linked to the nature of magma supply, and likely impact the upper crustal structure (section 5.2). An examination of available multibeam bathymetry along the global MOR reveals numerous central volcanoes with rift valleys at different stages of rifting. We propose a general model of central volcano emplacement and rifting based on similarities in the temporal evolution of these structures compared to Lucky Strike (section 5.3).

In the following sections, we use the spreading age, based on distance to the axis in the spreading direction and a full spreading rate of ~20 km/Myr, as a proxy of actual age. This provides a relative timing and duration of tectonic (e.g., graben formation) and volcanic events (e.g., volcano emplacement) [e.g., *Dusunur*, 2008], while absolute ages cannot be constrained with available data, as they would require extensive sampling and dating that is unavailable. In the case of grabens, the age derived from the distance between the graben edges (bounding faults) provides an upper estimate of the actual rifting age, as this method assumes pure magmatic accretion following the rift initiation. This assumption also obviates that grabens have a certain width at the time of their formation, a parameter that we cannot constrain, and hence the spreading age overestimates the actual age by a few tens of thousands of years. For example, if we consider a ~0.5 km wide initial graben, the spreading age would overestimate the actual age by ~25 kyr. Similarly, volcanic cones are constructed over older oceanic seafloor, and the spreading age we report corresponds to the distance between the center of the volcanic cone to its edge along a flow line. If the volcano emplacement takes place over preexisting seafloor, and associated with high effusion rates, the spreading ages necessarily overestimate the age of volcano emplacement.

5.1. History of Emplacement and Rifting of the Lucky Strike Seamount

Figure 10 synthesizes the main volcanic and structural features at the center of the Lucky Strike segment (Figures 10a and 10b), that we use to constrain the history of this central volcano (Figure 10c). From the profiles across the summit of the Lucky Strike seamount, the rift valley floor (*rf*), defined by the base of the rift

Table 2. Central Volcanoes Along the Global MOR System and Their Characteristics

Ridge	Site[a]	Latitude[a]	Longitude	Radius[b], km	Height[c], m	Rift Width[d], km	Volume[e], km^3
Spiess R.	Idem	54.7°S	0.1°E	7.5	700	Unrifted	41
SWIR	11°E	52.8°S	11.3°E	7.0	1600	8.9	82
	34°E	46.1°S	34.3°E	4.8	660	4	16
MAR	26°S	26.0°S	13.9°W	5.3	225	1.1	7
	18°N	18.3°N	46.7°W	6.1	905	7.8	35
	Lucky Strike	37.3°N	32.3°E	4.0	450	3.9	8
	v1	″	″	0.8	150	0.6	0.09
	Menez Gwen	37.8°N	31.5°W	6.6	830	2.4	38
	38°N	38.3°N	30.7°W	14.0	1440	3.5	295
JdF	47.5°N	47.6°N	129°W	3.0	565	4.0	5
SEIR	24°S	24.5°S	69.9°E	4.7	1100	2.8	25
Mariana	17°N	17.0°N	144.9°E	5.0	485	10.1	13
Red Sea[f]	Habita Mons	22.2°N	37.9°E	11.0	530	1.0–5.0	67
	Aswad	20.9°N	38.2°E	8.9	470	2.5-5.0	39
	Thetis	22.7°N	37.6°E	7.7	370	4.0–6.0	23
	Mabahiss	25.5°N	36.1°E	6.7	260	Unrifted	12
Bransfield	The Axe	62.9°S	59.8°W	7.5	450	3.5	27

[a]For each site, the latitude and longitude of the volcano center is provided. SWIR: South-West Indian Ridge; MAR: Mid-Atlantic Ridge; JdF: Juan de Fuca; SEIR: Southeast Indian Ridge; Mariana: Mariana Back arc. Red Sea: Red Sea Ridge; Bransfield: Bransfield back-arc basin. Bathymetry obtained from MGDS (http://www.marine-geo.org), except for Lucky Strike (this study), the Red Sea [*Augustin et al.*, 2014] and Bransfield Back-arc ridge [*Aquilina et al.*, 2013].

[b]Volcano radius is measured across axis, and between the edge of the central graben and the edge of the volcano as identified in the bathymetry (e.g., profile sections highlighted in red, Figure 12c).

[c]Reported height corresponds to the difference between the shallowest and deepest profile section across the volcano flanks (red in Figure 12c).

[d]Rift width corresponds to the distance between the top of bounding rift walls as identified in the across-axis bathymetric profiles (profile sections highlighted in black, Figure 12c).

[e]Volume is calculated from the radius and height, assuming a conical shape, and rounded to the nearest integer in km^3 for all volcanoes except Lucky Strike summital cone *v1*.

[f]From bathymetry published by *Augustin et al.* [2014]. Habita Mons is flanked by salt glaciers and the across-axis profile is not shown in Figure 12.

bounding walls (*rw*), has a width of ∼10 km, which corresponds to a spreading age of ∼500 kyr. The clear basal limit of the central volcano (*vf*) indicates an emplacement on a preexisting rift valley floor with a maximum spreading age of ∼320 kyr. The wider, older graben (*rb* in Figure 10a) dissecting the seamount has a width at the segment center of ∼3–4 km (Profiles B and A, respectively in Figure 10b), and its limits correspond to faults that are imaged in seismic reflection profiles to a depth of ∼500–700 m b.s.f. [*Combier*, 2007; *Singh et al.*, 2006; *Arnulf et al.*, 2014]. The *rb* graben edges thus correspond to spreading ages of ∼200–150 kyr, and consequently the emplacement of the volcano must have occurred between this spreading age and ∼300 kyr. Within this older graben *rb*, a second and more recent axial graben *ra* (Figure 10) extends ∼10 km along axis.

We observe the emplacement within the older graben *rb* of two summital volcanic cones, *v1* and *v2* in Figure 10. These cones, cross-cut by the recent graben *ra*, are at different rifting stages (Figure 10a). The older volcanic cone *v2* (Profile A-A′, Figure 10b) has a width of ∼2.5 km, corresponding to ∼125 kyr, has been fully dissected by the axial graben *ra*, which has a width of ∼1.2 km (∼60 kyr) and a total relief of ∼150 m. The more recent volcanic cone *v1* has a width of ∼1.5 km and was emplaced after axial graben *ra* was initiated, fully infilling it, and extending beyond its limits. Continued extension along this graben *ra* is visible in the set of faults that crosscut this later cone defining a ∼600 m wide graben with no significant relief (Profile B-B′, Figure 10b). The ages of emplacement of *v1* are thus bound by the initiation of rifting for graben *ra* along profile BB dissecting *v2* (60 kyr) and the spreading age corresponding to the width of *ra* across the summit of *v1* (30 kyr). Figure 10c summarizes this relative timing of volcanic and tectonic events based on spreading ages, with triangles indicating rifting events and dashed lines spanning the possible periods of ongoing rifting/spreading and volcanic emplacement.

Fast rates of magmatic rmplacement at the seafloor are consistent with the anomalously thick Layer 2A, its low velocity, and the presence of internal reflectors, which probably represent different phases of volcano emplacement volcanically buried [*Arnulf et al.*, 2014]. The lack of faulting and fissuring on the volcano flanks (*vf* in Figure 10) suggests that the emplacement of the Lucky Strike seamount was rapid relative to tectonic

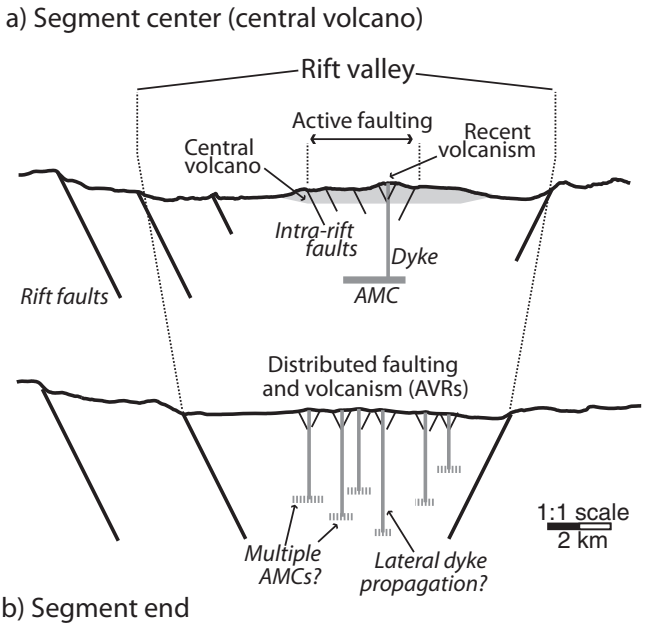

Figure 11. Cartoon showing differences in mode of volcanic emplacement and faulting between (a) the central volcano at the segment center and (b) the rift valley away from the central volcano. At the Lucky Strike volcano summit, recent volcanism and faulting are restricted to a well-defined axial graben (Figure 10). At the segment end, volcanism and deformation is distributed throughout the rift valley floor, and lacks a clear zone of preferential accretion. Volcanic ridges dominate volcanism, and can result from either lateral propagation of dikes from the central volcano and its underlying magma chamber, or from small, local magma chambers.

extension during the same period of time, and that faults were efficiently buried by lava. This volcanic masking of tectonic deformation is well documented along the East-Pacific Rise axis, where the seafloor is frequently repaved [*Escartín et al.*, 2007]. We suggest that the actual time of emplacement of the volcanic units is probably a fraction of the time given by spreading ages (solid lines in Figure 10c, indicated for illustration purposes).

Excess effusion rates can be estimated from the duration of volcanic emplacement of both the main Lucky Strike volcano and its summit volcanic cones. As the duration of emplacement, based on spreading age, is likely a maximum estimate of the actual value, the effusion rates given below are necessarily minimum estimates. For the Lucky Strike central volcano, the emplacement age (120–170 kyr) and the volcano volume (8 km^3, Table 2) yields effusion rates of 47–67 km^3/Myr. The summital volcanic cone *v1*, with an emplacement age of ~30 kyr and a volume of ~0.09 km^3 (Table 2), yields effusion rates of only 3 km^3/Myr, an order of magnitude lower than the estimate for the longer-term Lucky Strike volcano emplacement; rates associated with the rifted *v2* are not as well constrained, but are similar to those of *v1*. The estimated effusion rates are thus low with respect to a melt supply of ~140 km^3/Myr per km of ridge axis required to construct a 7 km thick crust at the center of the Lucky Strike segment [*Crawford et al.*, 2010], and may be accommodated by moderate fluctuations in melt supply to the segment center. Actual effusion rates associated with volcanic emplacement may however be significantly higher if the spreading age overestimates significantly the emplacement age.

5.2. Along-Axis Variations in Melt Delivery, Deformation, and Upper Crust Construction

Comparison of the bathymetry and volcano-tectonic structure between profile C-C′ and the two summit profiles (A-A′ and B-B′, Figure 10, see also Figure 8), clearly shows a transition in the overall seafloor structure away from the volcanic center, corresponding to a change in mode of upper crust construction as illustrated in Figure 11. The most recent volcanic activity at the segment center is confined within the actively forming, ~1 km wide axial graben (*ra*). Away from the segment center, recent volcanism is more distributed, spreading over a ~4 km wide zone throughout the rift valley (Figure 8a, Profile C-C′ in Figure 10). To either side of Lucky Strike seamount, on the rift valley floor, volcanic activity is dominated by emplacement of individual axial volcanic ridges, whereas at the segment center volcanic activity is dominated by sheet flows restricted to the most recent graben. Based on our morphological interpretation, the relative proportion of sheet-to-pillow flows is ~0.45 on Lucky Strike volcano and ~0.11 away from the influence of volcanic vents associated with the volcano (Figure 8c).

Faulting patterns also change along the segment. At the segment center, the narrow graben is dominated by inward-facing faults suggesting localized and organized extension linked to volcanic emplacement. Away from the segment center, faults fan out and spread over a much wider area of the rift valley floor, with scarps facing both eastward and westward. In these zones north and south of the volcano, the locus of present day or recent deformation is not well defined.

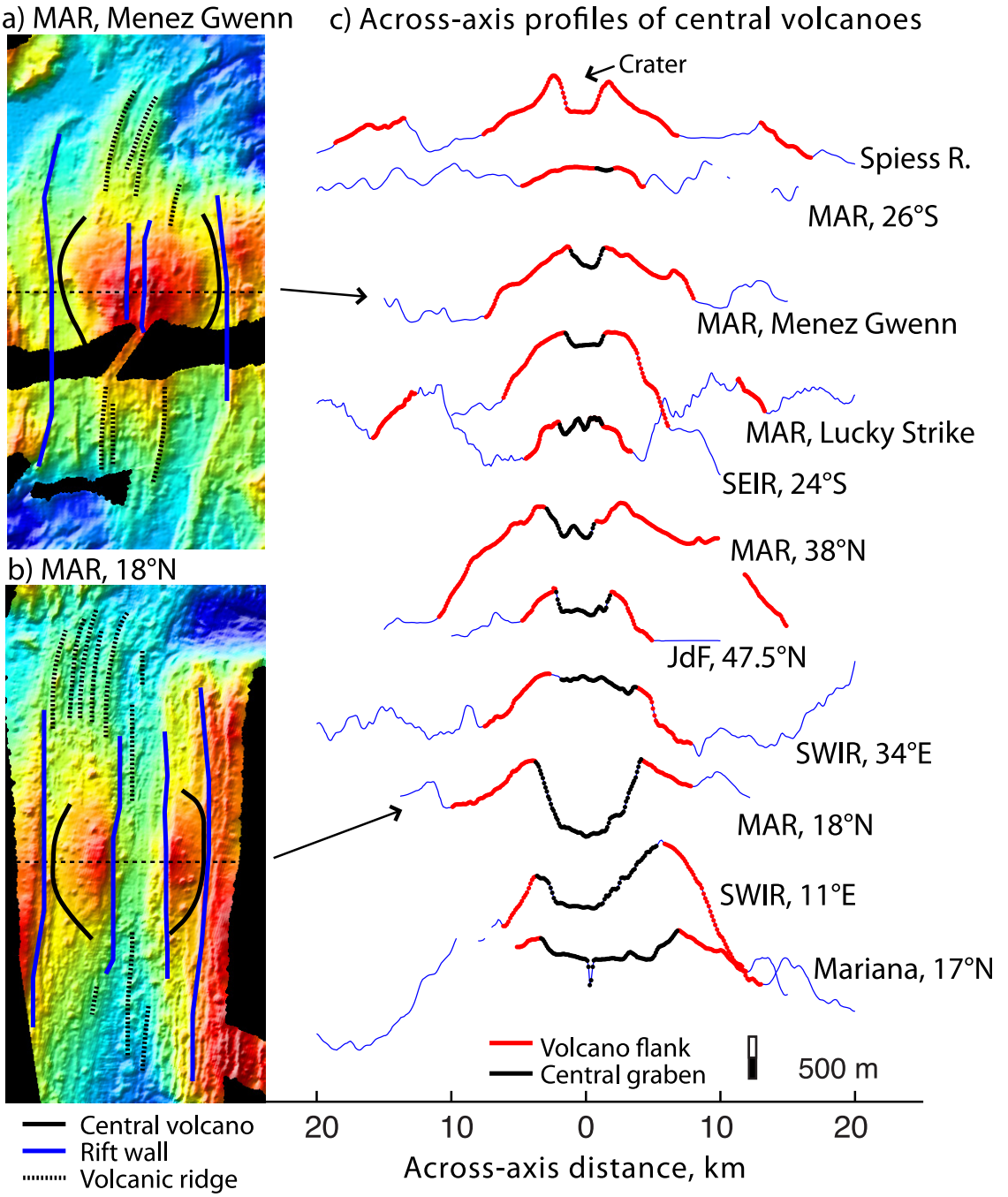

Figure 12. Examples of central volcanoes along the Mid-Atlantic Ridge, at an (a) initial stage of rifting (Menez Gwen segment) and (b) advanced stage with the onset of normal seafloor spreading (MAR, 18°N). (c) Across-axis profiles through the center of central volcanoes (see Table 2), showing the unrifted flanks (red) and the axial graben (black). Profiles are arranged according to axial graben width, increasing from top to bottom. Bathymetry profiles were extracted from the Global Multi-Resolution Topography synthesis [*Ryan et al.*, 2009].

Finally, we suggest that both the emplacement of the main volcanic edifice and the later volcanic cones at its summit, as well as the development of a narrow axial graben (*ra* at the present time), are most likely linked to the presence of an axial magma chamber that is long lived. First, the central volcano buildup requires efficient magma pooling and delivery to the seafloor initiating as dikes that likely focus to a point source. This mode of volcanic emplacement is suggested by the distribution of volcanic facies (Figure 8b) and the presence of sheet flows within the axial graben, and differs profoundly from the accretion involving AVRs commonly found at slow spreading MORs, that imply repeated fissure eruptions instead. Second, the most recent graben has a limited along-axis length of ~10 km, and its termination with the fanning of faults

and the distribution of volcanism through a wider rift valley floor area is in close proximity to the northern and southern limits of the AMC (Figure 10a). The faults bounding the ~1 km wide graben can only penetrate the uppermost crust, and hence cannot root at or near the ~3.5 km deep AMC [e.g., *Barreyre et al*., 2012]. Instead, these faults are likely linked to surface deformation associated with dike emplacement sourcing from the AMC.

Along-axis and away from the AMC, lithospheric thickness increases, resulting in a broader zone of deformation, and a transition that requires the fanning of faults between these two environments (Figure 8). The pillow lava flow morphologies that are most common in these areas indicate lower effusion rates than at the segment center. The lack of correlation between AVR inferred age and degree of tectonic disruption suggests that deformation is distributed across the axial valley floor, consistent with the fanning of faults away from the central volcano. In this environment, small-scale faulting associated with dike emplacement and limited extension would then be distributed throughout the zone of dike emplacement, and result in a fault pattern that shows no clear organization in fault-facing direction (see Figure 10c), in contrast to the deformation dominated by inward-facing faults at the volcano summit (Figure 11). Hydroacoustic monitoring in the area [*Smith et al*., 2003, 2002] recorded a seismic swarm in 2001. A 30 min long tremor at the onset of the event, and the lack of T-phases suggesting a tectonic event, led *Dziak et al*. [2004] to conclude that the event was associated with a dike emplacement. We anticipate that these two modes of volcanic construction produce extrusive layers with markedly different types of lavas and flows.

There are two possible models for the formation of AVRs found away from the volcano summit. Melt could be sourced from the central AMC, and propagate laterally through diking and fissure eruptions; AVRs abutting the base of central volcanoes elsewhere are visible in the bathymetry (Figure 12). Alternatively, a central AMC may coexist with smaller and shorter-lived magma supply for individual AVRs, as suggested for other MAR segments [*Smith and Cann*, 1993]. This second model is consistent with basalt geochemistry from the Lucky Strike suggesting several melt sources along the ridge axis [e.g., *Gale et al*., 2011; *Moreira et al*., 2011]. In this second model, small-scale faulting associated with dike emplacement away from the volcano center would accommodate a limited amount of extension, and would then result in a heterogeneous fault pattern showing no clear organization in fault-facing direction (see Figure 9c). This is in contrast to the deformation dominated by inward-facing faults at the volcano summit (Figure 10).

5.3. Life Cycle of Central Volcanoes Within the MOR Valley

The pattern of rapid volcano emplacement within a well-formed rift valley and its subsequent rifting is not restricted to the Lucky Strike seamount, and may be applicable to other central volcano seamounts found along the global MOR system. Table 2 summarizes the location and characteristics of 16 major central volcanoes within the MOR rift valley identified from available bathymetry data at the Marine Geoscience Data System (http://www.marine-geo.org). Figure 12 shows bathymetric profiles across some of the seamounts in Table 2, together with bathymetric maps for the Menez Gwen and 18°N segments at the MAR. All central volcanoes identified have well-defined basal limits (in the across-axis direction) that are often close to the fault scarps bounding the rift valley. With the exception of the unfaulted Spiess Ridge and Mahabiss (Red Sea) volcanoes (Table 2), the rest display a central graben bisecting the edifices through their summit; profiles in Figure 12c are arranged according to graben width as proxy for its development.

As in the case of the Lucky Strike seamount, the flanks of volcanoes are unfaulted and well preserved. Incipient grabens (narrow and with low relief), such as the one at Menez Gwen (Figure 12a) or graben *ra* at Lucky Strike (Figure 10), have limited along-axis extent and do not fully dissect the whole volcanic edifice. If a graben develops further, the central volcano is dissected and regular seafloor accretion develops (e.g., MAR at 18°N, Figure 12b), thereby rafting the volcano flanks apart while preserving them.

The bathymetric data also show that central volcanoes lack a well-defined termination in the along-axis direction. It is common to observe a gradual transition toward "normal" seafloor, often showing AVRs linking and possibly rooting at the volcanic edifice. This rooting would indicate redistribution of melt from the seamount center through diking. Alternatively, AVRs could have formed prior to the volcano emplacement and are now covered by it, although based on the morphology and continuity of structures, we suggest that their formation is related to the central volcano's growth.

The similarities in structure and evolution among the different edifices presented in Table 2 and the Lucky Strike seamount suggest a common process of formation and evolution shared by these features. The

emplacement of a central volcano is necessarily rapid, requiring enhanced melt supply at the segment center. This volcanic construction is likely associated with a long-lived AMC that stores melt and feeds eruptions that focus at the seafloor, over extended periods of time (tens to hundreds of thousands of years), likely associated with hydrothermal activity. This volcanic phase is then abruptly terminated, with deformation localizing along a central graben that dissects the volcano, preserving its unfaulted flanks (Figure 12c).

Off-axis bathymetric data (outside the rift valley) at Lucky Strike reveal three successive episodes of central volcano emplacement and subsequent rifting (Figures 1 and 12c) along a flow line, and with a spacing of 10–15 km, corresponding to a recurrence time of ~1–1.5 Myr. Similar cyclicity is also identified in the off-axis bathymetry at the Spiess Ridge seamount. In contrast, off-axis observations along the SWIR [*Cannat et al*., 2006] show instead that enhanced melt production in other areas may not fixed to specific locations along the axis. Elsewhere, due to the lack of bathymetry data off axis, it is not possible to evaluate if this recurrence is pervasive, implying a long-lived mantle anomaly as would be the case for Lucky Strike and Spiess Ridge, or if central volcanoes are generally isolated events with no cyclic behavior, as in the case for the SWIR, suggesting instead the processing at the ridge axis of mantle heterogeneities of restricted size.

The formation of central volcanoes involves the focused emplacement of large volumes of melt to the seafloor. Precisely estimates, the volume of the original edifices, are difficult owing to rifting. However, a minimum volume estimate can be obtained assuming a conical shape, with the height and radius reported in Table 2. The radius is estimated in the across-axis direction, between the edge of the central graben and the edge of the volcano, which can be clearly identified in the bathymetry (e.g., profile sections highlighted in red, Figure 12c). The along-axis extent of the volcano is less clear, owing to the interaction of the volcano emplacement and accretion along the ridge axis. The volume estimates in Table 2 are thus a minimum, as edifices are often elongated along axis, and this is confirmed by the comparison of these volume estimates with those derived from multibeam bathymetry. In the case of Menez Gwen, assuming an arbitrary isobath as the volcano base, the calculated volume of ~75 km^3 is larger than the 60 km^3 estimated using a conical shape. Volumes for volcanoes in Table 2 range from a few to a few hundred cubic kilometers (e.g., ~8 km^3 for Lucky Strike, >250 km^3 for MAR 38°N, Figure 12c).

Lacking seismic experiments, there is no constraint on the volume of magma chambers at central volcanoes along slow spreading ridges, except for the Lucky Strike volcano. Here we estimate that the maximum volume of melt within the Lucky Strike AMC underlying the central volcano is ~1 km^3 or less: the AMC reflector extends ~6 km along and ~3 km across axis [*Combier*, 2007; *Singh et al*., 2006], over an area of ~10 km^2, and we assume a maximum thickness of 100% melt lens of ~100 m, based on results from the EPR [*Collier and Singh*, 1997; *Singh et al*., 1999]. Therefore, the volume of melt in the present-day AMC exceeds amount of melt required to construct one of the summital cones (0.09 km^3 for *v1*, Table 2). Construction of central volcanoes identified along the axis of slow and ultraslow spreading segments thus requires a period of sustained melt supply transiting through the melt lens, with successive episodes of AMC replenishment and eruptions to the seafloor. The cessation or decrease in the melt supply and/or the rate of AMC replenishment can thus lead to the development of axial rift graben. If melt supply diminishes sufficiently, the onset of regular seafloor spreading can ultimately result in the splitting of the central volcano.

6. Conclusions

An analysis and interpretation of sidescan sonar imagery, coupled with that of optical seafloor imagery, informs us of the constructional and deformational history of Lucky Strike seamount. This provides a model to explain the characteristics and temporal evolution of other central volcanoes found along mid-ocean ridges. The Lucky Strike central volcano was emplaced within a preexisting rift valley, rising ~500 m or more above surrounding seafloor, as a result of a phase of high effusive rates. In general, volcanic output during central volcanic construction is sufficient to bury any tectonic features (faults, fissures) associated with plate separation, as indicated by the unfaulted nature of volcano flanks preserved on and off axis. Based on volumes of these edifices (from a few to more than a hundred cubic kilometers), we infer that this phase of volcanism must involve either a continuous melt supply, or the succession of numerous replenishment of and eruption events from an underlying magma chamber. The conic nature of these edifices and the evidence from volcanic acoustic facies of a concentric structure around the summit of Lucky Strike indicates that the focusing of melt is efficient. Decrease in the rate of melt supply may promote the formation

of a new axial graben at the summit of the volcano. If sustained, this decrease in melt supply can result in a widening of this incipient rift, the onset of regular seafloor spreading within it, and the rafting of unfaulted volcano flanks off axis.

Central volcanoes are associated with important along-axis changes in the nature of volcanic upper crustal construction and the distribution of deformation (primarily at slow and ultraslow spreading MORs), reflecting both the presence of an AMC (and a thin lithospheric lid above it) and the thickening of the lithosphere toward the segment ends. Within the rift valley, axial grabens formed at central volcanoes are narrow and well defined at the center (volcano summit), bound by inward-facing faults. Away from the volcano center, these structures widen and eventually disappear, with deformation being distributed throughout a wide area of the rift valley. Sonar imagery at Lucky Strike suggests that this tectonic change also correlates with a variation in the volcanic style. At the volcano summit, recent volcanism is constrained to the narrow axial graben, and is dominated by high effusion rate sheet flows. Away from the central volcano, the seafloor is dominated by pillowed axial volcanic ridges which reflect eruptions with low effusion rates. Volcanic ridges are present throughout the width of the rift valley and lack of an age progression, indicating that the zone of emplacement is wide, poorly defined, and possibly associated with a thick lithosphere in the absence of an AMC in the mid or shallow crust. These dikes can be sourced at the central volcano through lateral dike propagation, or be fed by ephemeral local magma chambers; both modes of volcanic ridge formation may coexist. The mode of rapid central volcano emplacement and subsequent rifting that we have documented at Lucky Strike is common along the MOR system. These volcanic events require transient mechanisms of melt focusing, accumulation, and transport to the seafloor, likely associated with a long-lived melt lens.

Acknowledgments

We thank the captain, officers, crews, and science parties of R/V Knorr during Cruise Lustre'96 (funded by NSF), and N/O Atalante during Graviluck'06 cruise (funded by CNRS/IFREMER). The *TowCam* delployment for seafloor imaging during the Graviluck'06 cruise was supported by NSF grant OCE-0623744 to A.S. and D.J.F., and by WHOI Deep Ocean Exploration Institute funding (AS & DF). D.J.F. also benefitted from a visiting position at IPGP to carry out this work. The field data acquisition for the Lustre'96 cruise was supported by NSF grant OCE-9505579. The Flores, Sudaçores, and SISMOMAR cruises where funded by CNRS/IFREMER (France). Material available on line through the Marine Geoscience Datasystem (http://www.marine-geo.org) includes the sonar grids (mosaics and individual sonar tracks) at full resolution (http://www.marine-geo.org/tools/search/Files.php?data_set_uid=21460) and the fault and fissure data (http://www.marine-geo.org/tools/search/Files.php?data_set_uid=21461). Comments and suggestions by the Associate Editor T. Becker, N. Augustin, and two additional anonymous reviewers, helped improve this manuscript. This is IPGP contribution 3578.

References

Aquilina, A., D. P. Connelly, J. T. Copley, D. R. H. Green, J. A. Hawkes, L. E. Hepburn, V. A. I. Huvenne, L. Marsh, R. A. Mills, and P. A. Tyler (2013), Geochemical and visual indicators of hydrothermal fluid flow through a sediment-hosted volcanic ridge in the Central Bransfield Basin (Antarctica), *PLoS One*, *8*, e54686.

Arnott, S. K., and G. R. Foulger (1994a), The Krafla spreading segment, Iceland 1, Three-dimensional crustal structure and the spatial and temporal distribution of local earthquakes, *J. Geophys. Res.*, *99*(B12), 23801–23825.

Arnott, S. K., and G. R. Foulger (1994b), The Krafla spreading segment, Iceland: 2. The accretionary stress cycle and nonshear earthquake focal mechanisms, *J. Geophys. Res.*, *99*, 23,827–23,842.

Arnulf, A. F., A. J. Harding, G. M. Kent, S. C. Singh, and W. C. Crawford (2014), Constraints on the shallow velocity structure of the Lucky Strike Volcano, Mid-Atlantic Ridge, from downward continued multichannel streamer data, *J. Geophys. Res. Solid Earth*, *119*, 1119–1144, doi:10.1002/2013JB010500.

Asada, M., A. Deschamps, T. Fujiwara, and Y. Nakamura (2007), Submarine lava flow emplacement and faulting in the axial valley of two morphologically distinct spreading segments of the Mariana back-arc basin from Wadatsumi side-scan sonar images, *Geochem. Geophys. Geosyst.*, *8*, Q04001, doi:10.1029/2006GC001418.

Augustin, N., C. W. Devey, F. M. van der Zwan, P. Feldens, M. Tominaga, R. A. Bantan, and T. Kwasnitschka (2014), The rifting to spreading transition in the Red Sea, *Earth Planet. Sci. Lett.*, *395*, 217–230.

Barreyre, T., J. Escartín, R. Garcia, M. Cannat, E. Mittelstaedt, and R. Prados (2012), Structure, temporal evolution, and heat flux estimates from the Lucky Strike deep-sea hydrothermal field derived from seafloor image mosaics, *Geochem. Geophys. Geosyst.*, *13*, Q04007, doi:10.1029/2011GC003990.

Blondel, P. (2009), *Handbook of Sidescan Sonar*, 320 pp., Springer, Berlin.

Bohnenstiehl, D., and M. C. Kleinrock (1999), Faulting and fault scaling on the median valley floor of the trans Atlantic geotraverse (TAG) segment, ~26°N on the Mid-Atlantic Ridge, *J. Geophys. Res.*, *104*, 29,351–29,364.

Briais, A., H. Sloan, L. M. Parson, and B. J. Murton (2000), Accretionary processes in the axial valley of the mid-Atlantic ridge 27°N-30°N from TOBI side-scan sonar images, *Mar. Geophys. Res.*, *21*, 87–119.

Cande, S. C., and D. V. Kent (1992), A new geomagnetic polarity time scale for the Late Cretaceous and Cenozoic, *J. Geophys. Res.*, *97*, 13,917–13,951.

Cann, J., and D. K. Smith (2005), Evolution of volcanism and faulting in a segment of the Mid-Atlantic Ridge at 25°N, *Geochem. Geophys. Geosyst.*, *6*, Q09008, doi:10.1029/2005GC000954.

Cannat, M., et al. (1999a), Mid-Atlantic ridge—Azores hotspot interactions: Along-axis migration of a hotspot-derived magmatic pulse 14 to 4 myrs ago, *Earth Planet. Sci. Lett.*, *173*, 257–269.

Cannat, M., C. Rommevaux-Jestin, D. Sauter, C. Deplus, and V. Mendel (1999b), Formation of the axial relief at the very slow spreading Southwest Indian Ridge (49°-69°E), *J. Geophys. Res.*, *104*, 22,825–22,843.

Cannat, M., D. Sauter, V. Mendel, E. Ruellan, K. Okino, J. Escartín, V. Combier and M. Baala (2006), Modes of seafloor generation at a melt-poor ultraslow-spreading ridge, *Geology*, *34*, 605–608.

Charlou, J. J., J. P. Donval, E. Douville, P. Jean Baptiste, J. Radford-Knoery, Y. Fouquet, A. Dapoigny, and M. Stievenard (2000), Compared geochemical signatures and the evolution of Menez Gwen (37°50′N) and Lucky Strike (37°17′N) hydrothermal fluids, south of the Azores Triple Junction on the Mid-Atlantic Ridge, *Chem. Geol.*, *171*, 49–75.

Collier, J., and S. C. Singh (1997), Detailed structure of the top of the melt body beneath the East Pacific Rise at 9°40′N from waveform inversion of seismic reflection data, *J. Geophys. Res.*, *102*, 20,287–20,304.

Combier, V. (2007), Mid-ocean ridge processes: Insights from 3D refection seismics at the 9°N OSC on the East Pacific Rise, and the Lucky Strike volcano on the Mid-Atlantic Ridge, PhD thesis, Inst. de Phys. du Globe de Paris, Paris.

Crawford, W. C., S. C. Singh, T. Seher, V. Combier, D. Dusunur and M. Cannat (2010), Crustal structure, magma chamber and faulting beneath the Lucky Strike hydrothermal fields, in *Diversity of Hydrothermal Sytems on Slow Spreading Ocean Ridges, Volume Diversity of Hydrothermal Sytems on Slow Spreading Ocean Ridges*, pp. 113–132, AGU, Washington, D. C.

Crawford, W. C., A. Rai, S. C. Singh, M. Cannat, J. Escartín, H. Wang, R. Daniel, and V. Combier (2013), Hydrothermal seismicity beneath the summit of Lucky Strike volcano, Mid-Atlantic Ridge, *Earth Planet. Sci. Lett.*, *373*, 118–128.

de Chabalier, J.-B., and J. P. Avouac (1994), Kinematics of the Asal Rift (Djibouti) determined from the deformation of Fieale volcano, *Science*, *265*, 1677–1681.

DeMets, C., R. G. Gordon, D. F. Argus, and S. Stein (1990), Current plate motions, *Geophys. J. Int.*, *101*, 425–478.

Deschamps, A., T. Fujiwara, M. Asada, L. Montesi, and P. Gente (2005), Faulting and volcanism in the axial valley of the slow-spreading center of the Mariana back arc basin from Wadatsumi side-scan sonar images, *Geochem. Geophys. Geosyst.*, *6*, Q05006, doi:10.1029/2004GC000881.

Detrick, R. S., H. D. Needham, and V. Renard (1995), Gravity anomalies and crustal thickness variations along the Mid-Atlantic ridge between 33°N and 40°N, *J. Geophys. Res.*, *100*, 3767–3787.

Dick, H. J. B., J. Lin, and H. Schouten (2003), An ultraslow-spreading class of ocean ridge, *Nature*, *426*, 405–412.

Dusunur, D. (2008), Thermal structure of mid-ocean ridges (Lucky Strike, Mid-Atlantic Ridge) and magma chambers, PhD thesis, 145 pp., Inst. de Phys. du Globe de Paris, Paris.

Dusunur, D., J. Escartín, V. Combier, T. Seher, W. Crawford, M. Cannat, M. Singh, L. M. Matias and J. M. Miranda (2009), Seismological constraints on the thermal structure along the Lucky Strike segment (Mid-Atlantic Ridge) and interaction of tectonic and magmatic processes around the magma chamber, *Mar. Geophys. Res.*, *30*, 105–120.

Dziak, R. P., D. K. Smith, D. R. Bohnenstiehl, C. G. Fox, D. Desbruyères, H. Matsumoto, M. Tolstoy, and D. J. Fornari (2004), Evidence of a recent magma dike intrusion at the slow spreading Lucky Strike segment, Mid-Atlantic Ridge, *J. Geophys. Res.*, *109*, B12102, doi:10.1029/2004JB003141.

Ebinger, C., and M. Casey (2001), Continental breakup in magmatic provinces: An Ethiopian example, *Geology*, *29*, 527–530.

Escartín, J., P. A. Cowie, R. C. Searle, S. Allerton, N. C. Mitchell, C. J. MacLeod, and A. P. Slootweg (1999), Quantifying tectonic strain and magmatic accretion at a slow spreading ridge segment, Mid-Atlantic Ridge, 29°N, *J. Geophys. Res.*, *104*, 10,421–10,437.

Escartín, J., M. Cannat, G. Pouliquen, A. Rabain, and J. Lin (2001), Crustal thickness of V-shaped ridges south of the Azores; interaction of the Mid-Atlantic Ridge (36°-39°N) and the Azores hot spot, *J. Geophys. Res.*, *106*, 21,719–21,735.

Escartín, J., S. A. Soule, D. J. Fornari, M. A. Tivey, S. Schouten, and M. R. Perfit (2007), Interplay between faults and lava flows in construction of the upper oceanic crust: The East Pacific Rise crest 9°25′-9°58′N, *Geochem. Geophys. Geosyst.*, *8*, Q06005, doi:10.1029/2006GC001399.

Escartín, J., et al. (2008a), Globally aligned photomosaic of the Lucky Strike hydrothermal vent field (Mid-Atlantic Ridge, 37°18.5′N): Release of geo-referenced data, mosaic construction and viewing software, *Geochem. Geophys. Geosyst.*, *9*, Q12009, doi:10.1029/2008GC002204.

Fornari, D. J. (2003), A new deep-sea towed digital camera and multi-rock coring system, *EOS Trans., AGU*, *84*, 69–73.

Fornari, D. J. et al. (2004), Submarine lava flow emplacement at the East Pacific Rise 9500N: Implications for uppermost ocean crust stratigraphy and hydrothermal fluid circulation in *Mid-Ocean Ridges: Hydrothermal Interactions Between the Lithosphere and Oceans*, vol. 148, edited by C. R. German and J. Lin, *Geophys. Monogr. Ser.*

Fornari D. J., K. L. Von Damm, J. G. Bryce, J. P. Cowen, V. Ferrini, A. Fundis, M. D. Lilley, G. W. Luther III, L. S. Mullineaux, M. R. Perfit, et al. (2012), The East Pacific rise between 9°N and 10°N: Twenty-Five Years of Integrated, Multidisciplinary Oceanic Spreading Center Studies, *Oceanography*, *25*, 18–43, doi:10.5670/oceanog.2012.02.

Fouquet, Y., J. L. Charlou, I. Costa, J. P. Donval, J. Radford-Knoery, H. Pellé, H. Ondréas, N. Lourenço, M. Ségonzac, and M. K. Tivey (1994), A detailed study of the Lucky Strike hydrothermal site and discovery of a new hydrothermal site: Menez Gwen; Preliminary results of the DIVAI Cruise (5–29 May, 1994), *InterRidge News*, *3*, 14–17.

Fouquet, Y., J. L. Charlou, I. Costa, J. P. Donval, J. Radford-Knoery, H. Pellé, H. Ondréas, N. Lourenço, M. Ségonzac, and M. K. Tivey (1994), A detailed study of the Lucky Strike hydrothermal site and discovery of a new hydrothermal site: Menez Gwen; Preliminary results of the DIVAI Cruise (5–29 May, 1994), *InterRidge News*, *3*, 14–17.

Gale, A., S. Escrig, E. J. Gier, C. H. Langmuir, and S. L. Goldstein (2011), Enriched basalts at segment centers: The Lucky Strike (37°17′N) and Menez Gwen (37°50′N) segments of the Mid-Atlantic Ridge, *Geochem. Geophys. Geosyst.*, *12*, Q06016, doi:10.1029/2010GC003446.

Gente, P., J. Dyment, M. Maia, and J. Goslin (2003), Interaction between the Mid-Atlantic Ridge and the Azores hot spot during the last 85 Myr: Emplacement and rifting of the hot spot-derived plateaus, *Geochem. Geophys. Geosyst.*, *4*(10), 8514, doi:10.1029/2003GC000527.

Gomez, O., A. Briais, D. Sauter, and V. Mendel (2006), Tectonics at the axis of the very slow spreading Southwest Indian Ridge: Insights from TOBI side-scan sonar imagery, *Geochem. Geophys. Geosyst.*, *7*, Q05K12, doi:10.1029/2005GC000955.

Gràcia, E., L. M. Parson, D. Bideau, and R. Hekinian (1998), Volcano-tectonic variability along segments of the Mid-Atlantic Ridge between the Azores platform and Hayes fracture zone: Evidence from submersible and high-resolution side-scan sonar data, in edited by R. A. Mills, and K. Harrison, pp. 1–15, Modern ocean floor processes and the geological record, Geological Society, London, U. K.

Head, J. W., L. Wilson, and D. K. Smith (1996), Mid-ocean ridge vent morphology and structure: Evidence for dike widths, eruption rates, and evolution of eruptions and axial volcanic ridges, *J. Geophys. Res.*, *101*, 28,265–28,280.

Hooft, E. E. E., R. S. Detrick, D. R. Toomey, J. A. Collins, and J. Lin (2000), Crustal thickness and upper mantle structure along three contrasting spreading segments of the Mid-Atlantic Ridge, *J. Geophys. Res.*, *105*, 8205–8226.

Humphris, S. E., D. J. Fornari, D. S. Scheirer, C. R. German, and L. M. Parson (2002), Geotectonic setting of hydrothermal activity on the summit of Lucky Strike seamount (37°17′N, Mid-Atlantic Ridge), *Geochem. Geophys. Geosyst.*, *3*(8), doi:10.1029/2001GC000284.

Klein, E. M., et al. (2013), Seafloor photo-geology and sonar terrain modeling at the 9°N overlapping spreading center, East Pacific Rise, *Geochem. Geophys. Geosyst.*, *14*, 5146–5170, doi:10.1002/2013GC004858.

Kuo, B. Y., and D. W. Forysth (1988), Gravity anomalies of the ridge-transform system in the South Atlantic between 31 and 31°S: Upwelling centers and variations in crustal thickness, *Mar. Geophys. Res.*, *10*, 205–232.

Langmuir, C., et al. (1997), Hydrothermal vents near a mantle hot spot: The Lucky Strike vent field at 37°N on the Mid-Atlantic Ridge, *Earth Planet. Sci. Lett.*, *148*, 69–91.

Lawson, K., R. C. Searle, J. A. Pearce, P. Browning, and P. Kempton (1996), Detailed volcanic geology of the MARNOK area, Mid-Atlantic Ridge north of Kane transform, in *Tectonic, Magmatic, Hydrothermal and Biological Segmentation of Mid-Ocean Ridges*, vol. 118, edited by C. J. MacLeod, P. A. Tyler, and C. L. Walker, pp. 61–102, Geol. Soc., London, U. K.

Lin, J., G. M. Purdy, H. Schouten, J. C. Sempere, and C. Zervas (1990), Evidence from gravity data for focused magmatic accretion along the Mid-Atlantic Ridge, *Nature*, *344*, 627–632.

Luis, J. F., and J. M. Miranda (2008), Reevaluation of magnetic chrons in the North Atlantic between 35N and 47N: Implications for the formation of the Azores Triple Junction and associated plateau, *J. Geophys. Res.*, *113*, B10105, doi:10.1029/2007JB005573.
Luis, J. F., J. M. Miranda, A. Galdeano, P. Paatriat, J. C. Rossignol, and L. A. Mendes Victor (1994), The Azores triple junction evolution since 10 Ma from an aeromagnetic survey of the Mid-Atlantic Ridge, *Earth Planet. Sci. Lett.*, *125*, 439–459.
MacLeod, C. J., R. C. Searle, J. F. Casey, C. Mallows, M. Unsworth, K. Achenbach, and M. Harris (2009), Life cycle of oceanic core complexes, *Earth Planet. Sci. Lett.*, *287*, 333–344.
Magde, L. S., A. H. Barclay, D. R. Toomey, R. S. Detrick, and J. A. Collins (2000), Crustal magma plumbing within a segment of the Mid-Atlantic Ridge, 35°N, *Earth Planet. Sci. Lett.*, *175*, 55–67.
Mendel, V., D. Sauter, C. Rommeveaux-Jestin, P. Patriat, F. Lefebvre, and L. M. Parson (2003), Magmato-tectonic cyclicity at the ultra-slow spreading Southwest Indian Ridge: Evidence from variations of axial volcanic ridge morphology and abyssal hills pattern, *Geochem. Geophys. Geosyst.*, *4*(5), 9102, doi:10.1029/2002GC000417.
Michael, P. J., et al. (2003), Magmatic and amagmatic seafloor generation at the utraslow-spreading Gakkel ridge, Arctic Ocean, *Nature*, *423*, 956–962.
Minshull, T. A., E. Morris, and R. S. Detrick (1995), Gravity anomalies and crustal structure at the Mesozoic Blake Spur fracture zone, *J. Geophys. Res.*, *100*, 17,771–17,779.
Miranda, J. M., J. F. Luis, N. Lourenço, and F. M. Santos (2005), Identification of the magnetization low of the Lucky Strike hydrothermal vent using magnetic data, *J. Geophys. Res.*, *110*, B04103, doi:10.1029/2004JB003085.
Mitchell, N. C. (1993), A model for attenuation of backscatter due to sediment accumulations and its application to determine sediment thicknesses with GLORIA sidescan sonar, *J. Geophys. Res.*, *98*(B12), 22477, doi:10.1029/93JB02217.
Mittelstaedt, E., S. Soule, K. Harpp, D. Fornari, C. McKee, M. Tivey, D. Geist, M. D. Kurz, C. Sinton, and C. Mello (2012), Multiple expressions of plume-ridge interaction in the Galápagos: Volcanic lineaments and ridge jumps, *Geophys. Geochem. Geosyst.*, *13*(5), Q05018, doi:10.1029/2012GC004093.
Moreira, M., J. Escartín, E. Gayer, C. Hamelin, A. Bezos, F. Guillon, and M. Cannat (2011), Rare gas systematics on Lucky Strike basalts (37°N, North Atlantic): Evidence for efficient homogenization in a long-lived magma chamber system?, *Geophys. Res. Lett.*, *38*, L08304, doi:10.1029/2011GL046794.
Okino, K., D. Curewitz, M. Asada, K. Tamaki, P. R. Vogt, and K. Crane (2002), Preliminary analysis of the Knipovich Ridge segmentation: Influence of focused magmatism and ridge obliquity on an ultraslow spreading system, *Earth Planet. Sci. Lett.*, *202*, 275–288.
Ondreas, H., Y. Fouquet, M. Voisset, and J. Radford-Knoery (1997), Detailed study of three contiguous segments of the Mid-Atlantic Ridge, South of the Azores (37°N to 38°30′N), using acoustic imaging coupled with submersible observations, *Mar. Geophys. Res.*, *19*, 231–255.
Ondréas, H., M. Cannat, Y. Fouquet, A. Normand, P.-M. Sarradin, and J. Sarrazin (2009), Recent volcanic events and the distribution of hydrothermal venting at the Lucky Strike hydrothermal field, Mid-Atlantic Ridge, *Geochem. Geophys. Geosyst.*, *10*, Q02006, doi:10.1029/2008GC002171.
Prados, R., R. Garcia, N. Gracias, J. Escartín, and L. Neumann (2012), A novel blending technique for underwater gigamosaicing, *IEEE J. Oceanic Eng.*, *37*, 626–644, doi:10.1109/JOE.2012.2204152.
Ribeiro da Costa, I., F. J. A. S. Barriga, C. Viti, M. Mellini and F. J. Wicks (2008), Antigorite in deformed serpentinites from the Mid-Atlantic Ridge, *European J. Mineralogy*, doi:10.1127/0935–1221/2008/0020–1808.
Ryan, B. F., et al. (2009), Global multi-resolution topography synthesis, *Geochem. Geophys. Geosyst.*, *10*, Q03014, doi:10.1029/2008GC002332.
Sauter, D., and M. Cannat (2010), The ultraslow spreading Southwest Indian Ridge, in *Diversity of Hydrothermal Sytems on Slow Spreading Ocean Ridges, Volume Diversity of Hydrothermal Systems on Slow Spreading Ocean Ridges, Geophys. Monogr. Ser.*, pp. 153–173, AGU, Washington, D. C.
Sauter, D., L. M. Parson, V. Mendel, C. Rommevaux-Jestin, O. Gomez, A. Briais, C. Mével, K. Tamaki, and FUJI Scientific Team (2002), TOBI sidescan sonar imagery of the very slow-spreading Southwest Indian Ridge: Evidence for along-axis magma distribution, *Earth Planet. Sci. Lett.*, *1999*, 81–95.
Sauter, D., H. Carton, V. Mendel, M. Munschy, C. Rommevaux-Jestin, J.-J. Schott, and H. Whitechurch (2004), Ridge segmentation and the magnetic structure of the Southwest Indian Ridge (at 55°30′E, 55°30′E and 66°20′E): Implications for magmatic processes at ultraslow-spreading centers, *Geochem. Geophys. Geosyst.*, *5*, Q05K08, doi:10.1029/2003GC000581.
Scheirer, D. S., D. J. Fornari, S. E. Humphris, and S. Lerner (2000), High-resolution seafloor mapping using the DSL-120 sonar system: Quantitative assessment of sidescan and phase-bathymetry data from the Lucky Strike segment of the Mid-Atlantic Ridge, *Mar. Geophys. Res.*, *21*, 121–142.
Searle, R. C., et al. (2010), Structure and development of an axial volcanic ridge: Mid-Atlantic Ridge, 45°N, *Earth Planet. Sci. Lett.*, *209*, 228–241.
Seher, T., W. C. Crawford, S. C. Singh, and M. Cannat (2010a), Seismic layer 2A variations in the Lucky Strike segment at the Mid-Atlantic Ridge from reflection measurements, *J. Geophys. Res.*, *115*, B07107, doi:10.1029/2009JB006783.
Seher, T., W. C. Crawford, S. C. Singh, M. Cannat, V. Combier and D. Dusunur (2010b), Crustal velocity structure of the Lucky Strike segment of the Mid-Atlantic Ridge at 37°N from seismic refraction measurements, *J. Geophys. Res.*, *115*, B03103, doi:10.1029/2009JB006650.
Seher, T., W. C. Crawford, S. C. Singh, M. Cannat, V. Combier, and D. Dusunur (2010c), Crustal velocity structure of the Lucky Strike segment of the Mid-Atlantic Ridge at 37°N from seismic refraction measurements, *J. Geophys. Res.*, *115*, B03103, doi:10.1029/2009JB006650.
Seher, T., S. C. Singh, W. C. Crawford, and J. Escartín (2010d), Upper crustal velocity structure beneath the central Lucky Strike Segment from seismic refraction measurements, *Geochem. Geophys. Geosyst.*, *11*, Q05001, doi:10.1029/2009GC002894.
Singh, H., C. Roman, O. Pizarro, R. Eustice, and A. Can (2007), Towards high-resolution imaging from underwater vehicles, *Int. J. Robotics Res.*, *26*, 55–74.
Singh, S. C., J. S. Collier, A. J. Harding, G. M. Kent, and J. A. Orcutt (1999), Seismic evidence for a hydrothermal layer avobe the solid roof of the axial magma chamber at the southern East Pacific Rise, *Geology*, *27*, 219–222.
Singh, S. C., W. C. Crawford, H. Carton, T. Seher, V. Combier, M. Cannat, J. P. Canales, D. Düsünur, J. Escartín and J. Miranda (2006), Discovery of a magma chamber and faults beneath a Mid-Atlantic Ridge hydrothermal field, *Nature*, *442*, 1029–1032.
Smith, D. K., and J. R. Cann (1993), Building the crust at the Northern Mid-Atlantic Ridge, *Nature*, *348*, 152–155.
Smith, D. K., et al. (1995a), Mid-Atlantic ridge volcanism from deep-towed side-scan sonar images, 25°-29°N, *J. Volcanol. Geotherm. Res.*, *67*, 233–262.
Smith, D. K., S. E. Humphris, and W. B. Bryan (1995b), A comparison of volcanic edifices at the Reykjanes Ridge and the Mid-Atlantic Ridge at 24°-30°N, *J. Geophys. Res.*, *100*, 22,485–22,498.

Smith, D. K., M. A. Tivey, H. Schouten, and J. R. Cann (1999), Locating the spreading axis along 80 km of the Mid-Atlantic Ridge south of the Atlantis Transform, *J. Geophys. Res.*, *104*, 7599–7612.

Smith, D. K., M. Tolstoy, C. G. Fox, D. R. Bohnenstiehl, H. Matsumoto, and M. Fowler (2002), Hydroacoustic monitoring of seismicity at the slow-spreading Mid-Atlantic Ridge, *Geophys. Res. Lett.*, *29*(11), doi:10.1029/2001GL013912.

Smith, D. K., J. Escartín, M. Cannat, M. Tolstoy, C. G. Fox, D. Bohnenstiehl, and S. Bazin (2003), Spatial and temporal distribution of seismicity along the northern Mid-Atlantic Ridge (15°-35°N), *J. Geophys. Res.*, *108*(B3), 2167, doi:10.1029/2002JB001964.

Soule, S. A., J. Escartín, and D. J. Fornari (2009), A record of eruption and intrusion at a fast-spreading ridge axis: The axial summit trough of the East Pacific Rise 9°-10°N, *Geochem. Geophys. Geosyst.*, *10*, Q10T07, doi:10.1029/2008GC002354.

Tivey, M. A., and J. Dyment (2010), The magnetic signature of hydrothermal systems in slow spreading environments, in *Diversity of Hydrothermal Sytems on Slow Spreading Ocean Ridges, Volume Diversity of Hydrothermal Systems on Slow Spreading Ocean Ridges, Geophys. Monogr. Ser.*, pp. 43–66, AGU, Washington, D. C.